



# 1 The ABoVE L-band and P-band Airborne SAR Surveys

2 Charles E. Miller<sup>1</sup>, Peter C. Griffith<sup>2</sup>, Elizabeth Hoy<sup>3</sup>, Naiara S. Pinto<sup>1</sup>, Yunling Lou<sup>1</sup>, Scott Hensley<sup>1</sup>,  
3 Bruce D. Chapman<sup>1</sup>, Jennifer Baltzer<sup>4</sup>, Kazem Bakian-Dogaheh<sup>5</sup>, W. Robert Bolton<sup>6</sup>, Laura Bourgeau-  
4 Chavez<sup>7</sup>, Richard H. Chen<sup>1</sup>, Byung-Hun Choe<sup>8</sup>, Leah Clayton<sup>9</sup>, Thomas A. Douglas<sup>10</sup>, Nancy French<sup>7</sup>,  
5 Jean E. Holloway<sup>11</sup>, Gang Hong<sup>8</sup>, Lingcao Huang<sup>12</sup>, Go Iwahana<sup>6</sup>, Liza Jenkins<sup>7</sup>, John S. Kimball<sup>13</sup>,  
6 Tatiana Loboda<sup>14</sup>, Michelle Mack<sup>15</sup>, Philip Marsh<sup>16</sup>, Roger J. Michaelides<sup>17</sup>, Mahta Moghaddam<sup>5</sup>,  
7 Andrew Parsekian<sup>18</sup>, Kevin Schaefer<sup>12</sup>, Paul R. Siqueira<sup>19</sup>, Debjani Singh<sup>20</sup>, Alireza Tabatabaenejad<sup>5</sup>,  
8 Merritt Turetsky<sup>21</sup>, Ridha Touzi<sup>8</sup>, Elizabeth Wig<sup>22</sup>, Cathy J. Wilson<sup>23</sup>, Paul Wilson<sup>8</sup>, Stan D.  
9 Wullschleger<sup>20</sup>, Yonghong Yi<sup>1,24</sup>, Howard A. Zebker<sup>22</sup>, Yu Zhang<sup>8</sup>, Yuhuan Zhao<sup>5</sup>, Scott J. Goetz<sup>25</sup>

10

11 <sup>1</sup>Jet Propulsion Laboratory, California Institute of Technology, Pasadena, CA, 91109, USA

12 <sup>2</sup>NASA Goddard Space Flight Center / SSAI, Greenbelt, Maryland, USA

13 <sup>3</sup>NASA Goddard Space Flight Center / GST, Inc., Greenbelt, Maryland, USA

14 <sup>4</sup>Department of Biology, Wilfrid Laurier University, Waterloo, Ontario, Canada

15 <sup>5</sup>Department of Electrical Engineering, University of Southern California, Los Angeles, CA, USA

16 <sup>6</sup>International Arctic Research Center, University of Alaska Fairbanks, Fairbanks, AK 99775-7340 USA

17 <sup>7</sup>Michigan Tech Research Institute, Michigan Technological University, Ann Arbor, MI 48105 USA

18 <sup>8</sup>Canada Centre for Remote Sensing, Ottawa, Ontario K1A0E4, Canada

19 <sup>9</sup>Department of Earth & Planetary Sciences, Yale University, New Haven, CT, USA

20 <sup>10</sup>U.S. Army Cold Regions Research and Engineering Laboratory, Fort Wainwright, Alaska 99709 USA

21 <sup>11</sup>Department of Geography, University of Ottawa, Ottawa ON K1N 6N5, Canada

22 <sup>12</sup>National Snow and Ice Data Center (NSIDC), University of Colorado, Boulder, Colorado 80309-0449 USA

23 <sup>13</sup>NTSG, WA Franke College of Forestry & Conservation, The University of Montana, Missoula, Montana USA

24 <sup>14</sup>Department of Geographical Sciences, University of Maryland, College Park, Maryland 20742, USA

25 <sup>15</sup>Center for Ecosystem Science and Society and Department of Biological Sciences, Northern Arizona University, Flagstaff,  
26 AZ 86011 USA

27 <sup>16</sup>Department of Geography and Cold Regions Research Centre, Wilfrid Laurier University, Waterloo, Ontario, Canada

28 <sup>17</sup>Department of Geophysics, Colorado School of Mines, Golden, CO, USA

29 <sup>18</sup>Department of Geology & Geophysics, University of Wyoming, 1000 E University Ave., Laramie, WY, USA

30 <sup>19</sup>Department of Electrical and Computer Engineering, University of Massachusetts, Amherst, MA 01003-9284 USA

31 <sup>20</sup>Biological and Environmental Systems Science Directorate, Oak Ridge National Laboratory, Oak Ridge, Tennessee USA

32 <sup>21</sup>Ecology and Evolutionary Biology Department, University of Colorado Boulder

33 <sup>22</sup>Department of Geophysics, Stanford University, Stanford, CA, USA

34 <sup>23</sup>Earth and Environmental Sciences Division, Los Alamos National Laboratory, Los Alamos, New Mexico USA

35 <sup>24</sup>Joint Institute for Regional Earth System Science & Engineering, The University of California, Los Angeles, CA 90095-  
36 7228 USA

37 <sup>25</sup>School of Informatics, Computing, and Cyber Systems, Northern Arizona University, Flagstaff, AZ 86011 USA

38

39

40 *Correspondence to:* Charles E. Miller ([charles.e.miller@jpl.nasa.gov](mailto:charles.e.miller@jpl.nasa.gov))

41



42 **Abstract**

43 Permafrost-affected ecosystems of the Arctic-boreal zone in northwestern North America are  
44 undergoing profound transformation due to rapid climate change. NASA's Arctic Boreal Vulnerability  
45 Experiment (ABoVE) is investigating characteristics that make these ecosystems vulnerable or resilient  
46 to this change. ABoVE employs airborne synthetic aperture radar (SAR) as a powerful tool to  
47 characterize tundra, taiga, peatlands, and fens. Here, we present an annotated guide to the L-band and P-  
48 band airborne SAR data acquired during the 2017, 2018, 2019, and 2022 ABoVE airborne campaigns.  
49 We summarize the ~80 SAR flight lines and how they fit into the ABoVE experimental design. We  
50 provide hyperlinks to extensive maps, tables, and every flight plan as well as individual flight lines. We  
51 illustrate the interdisciplinary nature of airborne SAR data with examples of preliminary results from  
52 ABoVE studies including: boreal forest canopy structure from tomoSAR data over Delta Junction, AK  
53 and the BERMS site in northern Saskatchewan and active layer thickness and soil moisture data product  
54 validation. This paper is presented as a guide to enable interested readers to fully explore the ABoVE L-  
55 and P-band SAR data.

56  
57

58 **Short Summary**

59 NASA's Arctic Boreal Vulnerability Experiment (ABoVE) conducted airborne synthetic aperture radar  
60 (SAR) surveys of over 120,000 km<sup>2</sup> in Alaska and northwestern Canada during 2017, 2018, 2019, and  
61 2022. This paper summarizes those results and provides links to details on ~80 individual flight lines.  
62 This paper is presented as a guide to enable interested readers to fully explore the ABoVE L- and P-  
63 band SAR data.

64  
65

66 **Keywords:** Airborne Synthetic Aperture Radar (SAR), Interferometric SAR (InSAR), Polarimetric  
67 SAR (PolSAR), Tomographic SAR (tomoSAR), Arctic, tundra, taiga, boreal forest, permafrost, Arctic  
68 Boreal Vulnerability Experiment (ABoVE)

69  
70

71 **Copyright Statement:**

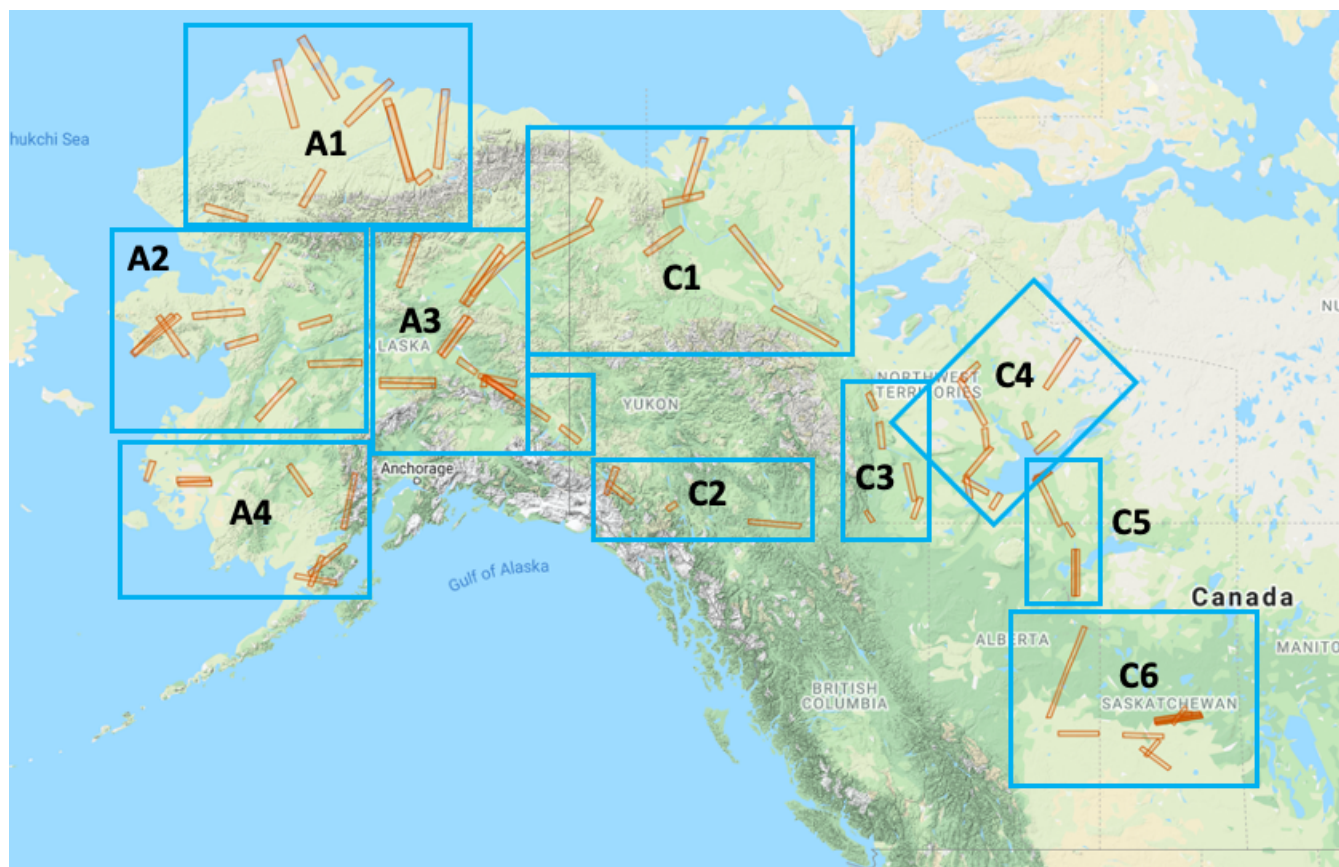
72 © California Institute of Technology. Government funding acknowledged.

73  
74  
75



76 **1 Introduction**

77 The Arctic region contains a remarkable diversity of cold-adapted biota, habitats, and permafrost-  
78 affected ecosystems [McGuire 2009; Vincent 2011]. As with other components of the Arctic system,  
79 Arctic ecosystems are strongly interdependent and the rapid degradation of the Arctic cryosphere is  
80 altering their physical, biogeochemical, and biological linkages in ways that may be irreversible  
81 [Vincent 2011; Hinzman 2013]. Understanding characteristics that make Arctic ecosystems vulnerable  
82 or resilient to this change is the overarching objective of NASA's Arctic Boreal Vulnerability  
83 Experiment (ABoVE, <https://above.nasa.gov/>). Miller et al. [2019] describes how airborne campaigns  
84 fit into the broader ABoVE research strategy and how the foundational synthetic aperture radar (SAR)  
85 measurements formed the framework around which all other airborne data acquisitions were planned.  
86  
87



88  
89 **Figure 1.** Flight lines for the L-band and P-band PolInSAR measurements capture critical bioclimatic, permafrost, and geographic  
90 gradients as well as key field sites and long-term measurement records across the 4 Mkm<sup>2</sup> ABoVE domain. The flight lines  
91 are collected into 10 composites which roughly correspond to the Alaskan (A1-A4) and Canadian (C1-C6) regions sampled on  
92 individual flight days. © Google Maps



93 ABoVE SAR flight lines (Figure 1) were planned to leverage legacy L- and P-band SAR transects  
94 acquired during the pre-ABoVE period; remotely-sensed permafrost active layer thickness time series  
95 derived from satellite interferometric SAR observations (ReSALT) [Schaefer 2015]; SAR data from  
96 PALSAR, PALSAR-2, RadarSat, RadarSat-2, and Sentinel-1; historic or planned airborne LiDAR  
97 acquisitions; and data from existing field sites [Hoy 2018]. Legacy airborne SAR flight lines include the  
98 L-band grid acquired over the Boreal Ecosystem Research and Monitoring Sites (BERMS) area near  
99 Prince Albert, SK during SMAP CanEx 2010 [Magagi 2012], the P-band lines over the BERMS area  
00 acquired from 2012-2015 during the Airborne Microwave Observatory of Subcanopy and Subsurface  
01 (AirMOSS) Earth Ventures Sub-orbital (EV-S1) investigation [Allen 2010; Moghaddam 2016], and a  
02 collection of 10 L- and P-band flight lines acquired over the Seward Peninsula, Northwestern Interior,  
03 and North Slope of Alaska during 2014 and 2015 [Chen 2019a, 2019b]. The BERMS area observations,  
04 in particular, link ABoVE to the Boreal Ecosystem–Atmosphere Study (BOREAS) studies of the 1990s  
05 [Sellers 1995; 1997].

06  
07 Hoy et al. [2018] compiled information on more than 6,700 field sites and previous remote sensing data  
08 sets to help plan the SAR flight lines and the ABoVE Airborne Campaigns [Miller 2019]. This  
09 compilation is intended to help investigators understand flight line choices and identify ground locations  
10 used to anchor individual flight lines. SAR data users may also search for the underlying data available  
11 within each flight line. Key anchor points for the SAR flight lines include: Active layer thickness  
12 measurements from the Circumpolar Active Layer Monitoring network (CALM); Permafrost  
13 temperatures and annual thaw depths from the Global Terrestrial Network for Permafrost (GTN-P)  
14 database; Soil moisture and permafrost state data from the Department of Energy’s Next Generation  
15 Ecological Experiment-Arctic (NGEE-Arctic) field sites on the Seward Peninsula and near Utqiagvik  
16 (formerly Barrow), AK; Extensive in situ terrestrial and aquatic ecosystem data as well as airborne  
17 LiDAR and spectral imagery from NSF’s National Ecological Observatory Network (NEON) D18  
18 tundra field sites near Utqiagvik (Barrow), AK and Toolik Lake, AK, and from the D19 taiga field sites  
19 near Caribou/Poker Creek, AK, Delta Junction, AK, and Healy, AK; Detailed ecological and physical  
20 climate time series from NSF’s Long Term Ecological Research (LTER) Arctic (Toolik Lake) and  
21 Boreal Forest (Bonanza Creek) sites; Long-term boreal forest inventory data from the Canadian  
22 Forestry Service’s (CFS) Climate Impacts on Productivity and Health of Aspen (CIPHA) and High  
23 Elevation & Latitude Climate Change Impacts & Adaptation (HEL CIA) plots; and Long term  
24 permafrost, hydrology and ecology time series records from the Canadian Changing Cold Regions  
25 Network (CCRN) sites at Trail Valley Creek, NWT, Havikpak Creek, NWT, Scotty Creek, NWT,  
26 Baker Creek, NWT, Wolf Creek Research Basin, YT, and the BERMS site at White Gull Creek, SK.

27  
28 Airborne SAR data enable numerous ecosystem and ecosystem change research investigations [NRC  
29 2014]. ABoVE researchers are using the airborne L- and P-band data to: Quantify permafrost active  
30 layer thickness and soil moisture content [Bakian-Dogahneh 2020]; Complement AirSWOT Ka-band  
31 acquisitions to determine water surface elevations in Arctic lakes, wetlands, and rivers [Pitcher  
32 2019a,b]; Investigate boreal forest and tundra fire scars, especially in conjunction with fire disturbance  
33 plots [Tank 2018; Walker 2018 a,b; 2019a,b; French 2020; Holloway 2020; Loboda 2021]; Map tree  
34 density and distribution across the Tundra-Taiga ecotone; Provide control point data for the ArcticDEM



35 [Porter 2018; Meddens 2018]; Investigate lidar-radar fusion remote sensing for boreal forest  
36 characterization as a precursor to NISAR/IceSAT-2 investigations [Silva 2021]; Quantify expansion and  
37 sediment mass flow from massive retrogressive thaw slumps – so-called megaslumps – on the Peel  
38 Plateau along the Dempster Hwy west of Fort McPherson [Kokelj 2013; 2015]; Classify Arctic  
39 wetlands and habitats [French 2020]; and Support algorithm development for NISAR (L-band) and  
40 BIOMASS (P-band) estimates of boreal forest structure and above ground biomass [Quegan 2019;  
41 Saatchi 2019]. Goetz [2021] summarizes how the ABoVE airborne SAR data are helping advance  
42 Arctic-boreal understanding and the remaining knowledge gaps still to be addressed.

43  
44 This paper presents an annotated guide to enable interested readers to fully explore the ABoVE L- and  
45 P-band SAR data acquired during the 2017, 2018, 2019, and 2022 ABoVE airborne campaigns. Section  
46 2 provides details on the L- and P-band SAR instruments and the flight line catalog. Section 3  
47 summarizes the daily sorties from each airborne campaign. Section 4 briefly describes the tomographic  
48 SAR (tomoSAR) experiments flown over Delta Junction, AK and the BERMS site near Prince Albert,  
49 SK. Section 5 describes some of the ABoVE SAR data products and their validation. Section 6  
50 highlights the synergies between the L- and P-band airborne SAR data and other airborne sensors.  
51 Section 7 summarizes access to the data products. Section 8 discusses potential future acquisitions and  
52 outlooks for exploiting these data. Additionally, we include an Appendix which describes the ~80  
53 ABoVE SAR flight lines and how each line fits into the ABoVE experimental design. The Appendix  
54 also provides extensive maps and tables for every flight plan and individual flight lines as well as a list  
55 of the acronyms and abbreviations. The Supplemental Information includes hyperlinked versions of the  
56 tables for direct access to flight lines and flight plans.

## 57 **2 The L-Band and P-band Airborne SAR Instruments and Data Acquisition**

58 Both the L- and P-band airborne SARs are sensitive to geometrical and material properties of  
59 vegetation, soil surface, and subsurface profiles [Saatchi and Moghaddam 2000; Tabatabaenejad 2011;  
60 Tabatabaenejad 2015]. The joint use of both L- and P-band gives enhanced sensitivity to near-surface  
61 (< 5 cm, L-band) and root zone (10-40 cm, P-band) portions of the subsurface profile compared to use  
62 of either wavelength alone [Du 2015]. Airborne acquisitions with both SARs provide 6-10 m spatial  
63 resolution, ~15 km swaths and transect lengths of 100 – 200 km, making them ideal for surveying  
64 above-ground biomass and vegetation canopy structure [Hensley 2014; 2016] as well as the tundra-taiga  
65 ecotone [Montesano 2016]. Special tomoSAR data were acquired over the well characterized BERMS  
66 site in northern Saskatchewan and the NEON site in Delta Junction, AK to quantify the performance of  
67 both SARs in reproducing the structure and biomass of boreal forests.

68

### 69 **2.1 The L-band SAR Instrument**

70 NASA's airborne L-band SAR (initially named the Uninhabited Aerial Vehicle Synthetic Aperture  
71 Radar (UAVSAR) system) is a compact pod-mounted polarimetric instrument for interferometric  
72 repeat-track observations that was developed at the NASA Jet Propulsion Laboratory (JPL) and Dryden



73 Flight Research Center (DFRC) in Edwards, CA. It operates at a center frequency of 1.2575 GHz  
74 (wavelength = 23.8 cm) with 80 MHz bandwidth. It is deployed on a Gulfstream III aircraft and images  
75 the Earth surface from a nominal 12.5 km altitude. The image swath is collected off-nadir in a ~22 km  
76 wide with incidence angles ranging from ~22°–67°. The instrument spatial resolution is 0.8m (along  
77 flight-line) by 1.7m (slant range, along line-of-sight (LOS) from the antenna to the ground).  
78 Topographic information is derived from phase measurements that, in turn, are obtained from two or  
79 more passes over a given target region. Its 1.26 GHz frequency results in radar images that are well-  
80 correlated from pass to pass. Polarization agility facilitates terrain and land-use classification.

81  
82 All L-band SAR data are publicly available at <http://uavsar.jpl.nasa.gov/> as individual InSAR products  
83 or as a single look complex (SLC) stack product of coregistered images for individual flight lines.  
84 Products are also available from the UAVSAR data portal at the Alaska SAR Facility Distributed  
85 Active Archive Center (<https://asf.alaska.edu/data-sets/sar-data-sets/uavsar/>). The L-band SAR provides  
86 key pre-launch algorithm development and validation data sets [Saatchi 2019] for the NASA-ISRO  
87 SAR (NISAR) mission [Rosen 2017].  
88

## 89 2.2 The P-band SAR Instrument

90 The P-band SAR was developed circa 2012 for the Earth Ventures Sub-orbital (EV-S1) Airborne  
91 Microwave Observatory of Subcanopy and Subsurface (AirMOSS) investigation [Allen 2010;  
92 Moghaddam 2016]. The radar is based on JPL's L-band UAVSAR system. The P-band SAR inherits  
93 UAVSAR's existing L-band RF and digital electronics subsystems. New up- and down-converters  
94 convert the L-band signals to UHF frequencies (280-440 MHz). The passive antenna is based on the  
95 legacy GeoSAR design [Chapin 2012].  
96

97 The P-band SAR was flown more than 1200 h from 2012 to 2015, covering regions of 2500 km<sup>2</sup> spread  
98 over nine major biomes in North America during the AirMOSS EV-S1 investigation [Tabatabaenejad  
99 2020]. Legacy acquisitions in Alaska [Chen 2019a, b] and over the BERMS site in northern  
00 Saskatchewan [Chapin 2012, 2018] provide an opportunity for extended time series analysis. All P-band  
01 SAR data are publicly available at <http://uavsar.jpl.nasa.gov/>. Additionally, ABoVE P-band SAR data  
02 will provide valuable insights into the characterization of boreal forest and tundra ecosystems by the  
03 upcoming BIOMASS mission [Le Toan 2011; Quegan 2019].  
04

## 05 2.3 The Platform Precision Autopilot (PPA) System

06 To support cm-precision interferometric land surface characterization, repeat pass measurements  
07 acquired by the SARs need to be taken from flight paths that are nearly identical. Both the L- and P-  
08 band SARs utilize real-time GPS that interfaces with the platform flight management system (FMS) to  
09 confine the repeat flight path to within a 10 m tube over a 200 km course in conditions of calm to light  
10 turbulence. The FMS is also referred to as the Platform Precision Autopilot (PPA). Additionally, the  
11 radar vector from the aircraft to the ground target area must be similar from pass to pass. This is



12 accomplished with an actively scanned antenna designed to support electronic steering of the antenna  
13 beam with a minimum of  $1^\circ$  increments over a range to exceed  $\pm 15^\circ$  in the flight direction.

14  
15 ABoVE SAR measurements were typically acquired with platform RMS deviations less than  $\pm 3$  m. Any  
16 platform deviations larger than  $\pm 10$  m from the programmed flight path resulted in the acquisition being  
17 terminated and a real time decision made to reacquire the line from the beginning or to continue with  
18 the flight plan and proceed to the next line. This decision balanced the science priority of the flight line,  
19 fuel consumption and remaining endurance, the number of flight lines yet to be acquired in the day's  
20 flight plan, distance from our base of operations, and whether there would be future opportunities to  
21 collect a given line by adding it to an upcoming flight plan. The flight team was extremely efficient in  
22 executing these decisions, resulting in 95% flight line acquisition success across the 2017-2019 period.  
23

#### 24 **2.4 Airborne SAR Flight Line and Flight Plan Designations**

25 The JPL SAR team devised a convenient and powerful way to identify airborne SAR data acquisitions  
26 for the Facility and PI instruments under their charge. Each L-band or P-band SAR flight line receives a  
27 unique 5-digit identifier consisting of the three-digit GPS compass heading followed by a two-digit  
28 index. A 6-character text string is also associated with each line for ease of identification. The text  
29 string precedes the numerical ID and usually provides abbreviated geographic or infrastructure  
30 information that characterizes the line. For example, L-band flight line Teller\_04901 identifies the flight  
31 line on the Seward Peninsula that overflies the Ngee-Arctic Teller watershed. The flight line identifier  
32 is a constant and, once assigned, is used whenever a line is reflown. In some cases, there are  
33 overlapping or nearly identical flight lines which differ slightly in their ID number. L-band and P-band  
34 flight lines use the same flight line identification system, allowing rapid identification of overlapping L-  
35 and P-band data acquisitions.

36  
37 Flight Plans are assembled from the composite flight lines for a given sortie. Each flight plan also  
38 receives a unique 5-digit identifier based on the year flown (digits 1 and 2) and the flight number for  
39 that year (digits 3-5). For example, L-band flight plan 17093 was flown in 2017 and was the 93<sup>rd</sup> sortie  
40 flown that year. Note that there may be more than one sortie flown on a given day, in which case each  
41 would have a unique flight plan identifier even though they were flown on the same calendar day and  
42 may include some or all of the same flight lines.

43  
44 In the Supplemental Information we provide hyperlinks to the JPL UAVSAR data portal  
45 (<https://uavsar.jpl.nasa.gov/cgi-bin/data.pl>). This provides links to the individual flight line data, maps,  
46 and related flight plans that acquired data over one or more of the individual flight lines. We hope this  
47 enables interested readers to explore the ABoVE L- and P-band SAR data more fully. These data and all  
48 other airborne data from the ABoVE campaigns may be explored on NASA's EarthData ABoVE Portal  
49 (<https://search.earthdata.nasa.gov/portal/above/search>). Ground sites used to design the orientation and  
50 locations of the flight lines are archived at the ORNL DAAC [Hoy 2018].  
51



### 52 3 The ABoVE Airborne SAR Campaigns

53 The L-band (Figure 2) and P-band (Figure 3) SARs were considered foundational measurements in the  
54 ABoVE airborne campaign strategy [Miller 2019]. The ~80 flight lines described in the Appendix  
55 formed the framework for the remainder of the airborne remote sensing acquisitions. The ABoVE SAR  
56 strategy was to execute same day acquisitions of both L- and P-band flight lines (Figure 1) for a given  
57 sortie during 2017 to optimize dual frequency retrievals; however, technical issues forced us to fly the  
58 instruments sequentially. The baseline L-band campaigns were flown in June (DOY 164-173) and  
59 September (DOY 251-263) of 2017 to characterize the land surface during periods of minimum and  
60 maximum active layer thickness, respectively. Subsequent L-band campaigns in 2018 (DOY 231-241),  
61 2019 (DOY 247-260) and 2022 (DOY 226-237) provide a time series synched to maximum annual  
62 active layer thickness. P-band campaigns were conducted in May-June (DOY 142-157) and August  
63 (DOY 219-227) of 2017. There was a 2-day P-band mini-campaign in October 2017 to extend the  
64 legacy time series of early cold season acquisitions over the Seward Peninsula, NW Alaska and North  
65 Slope Alaska (DOY 280-283).

66



67  
68  
69

Figure 2. Sahtu students Mandy Bayha (front left) and Joanne Speakman (front center) pose with their mentor Cindy Gilday (front right) and NASA flight crew in Yellowknife, NT after completing a L-band SAR survey flight around the Great Slave Lake





70  
71

Region on 22 August 2018 (Flight Plan 18048). This experience gave these Northerners a new appreciation for how NASA was helping understand, preserve, and protect their lands. Photo Credit: Stephen M. Fochuk, Government of Northwest Territories.

72  
73  
74



75

76  
77

Figure 3. The P-band SAR team with the NASA JSC G-III (N992NA) on the tarmac in Fairbanks, AK on 18 August 2017 after completing a survey of the Upper Mackenzie Valley (Flight plan 17083). Photo Credit: M. Moghaddam.

78



### 79 3.1 Alaskan Flight Lines

80 The Alaskan SAR flight lines are broken into four main regional collections: A1) North Slope Alaska,  
81 A2) Seward Peninsula and Northwest Alaska, A3) Eastern Interior, and A4) Southwest Alaska and the  
82 Yukon-Kuskokwim Delta (**Figure 1**). Individual flight  
83 lines were planned based on long-term ground  
84 monitoring sites [Hoy 2018], existing or planned field  
85 research, recent disturbances, important geographic or  
86 ecological gradients, complementary remote sensing  
87 data, and consultation with indigenous peoples and  
88 governments [Miller 2019]. Legacy L- and P-band flight  
89 lines from the AirMOSS EV-S1 investigation [Allen  
90 2010; Moghaddam 2016] in the Seward Peninsula, NW  
91 Alaska, and the North Slope were adapted for ABoVE  
92 use. Acquisition of P-band flight lines in the central  
93 Interior was not possible due to a military radar keep-out  
94 zone centered near Clear, AK. The keep-out zone is  
95 shown in all P-band flight plan maps (Ex. **Figure 4**).

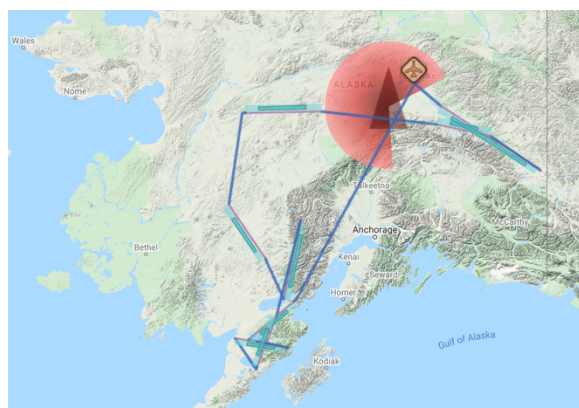


**Figure 4.** The military radar at Clear, AK creates a large P-band operations keep-out zone in the central Interior (red areas). The aircraft symbol marks our Fairbanks International Airport (PAFA) base of operations. Data acquisitions (blue bars) are from Flight Plan 17054. © Google Maps

### 97 3.2 Canadian Flight Lines

98 The Canadian SAR flight lines are broken into six regional collections: C1) Lower Mackenzie Valley  
99 and Northern Yukon Territory, C2) Southern Yukon Territory, C3) Upper Mackenzie Valley, C4) Great  
00 Slave Lake Region, C5) Transboundary Watershed, and C6) Southern Boreal Forest/BERMS.  
01 Individual lines were planned based on long-term ground monitoring sites [Hoy 2018], existing or  
02 planned field research, recent disturbances, important geographic or ecological gradients,  
03 complementary remote sensing data, and consultation with local inhabitants and governments [Miller  
04 2019]. Legacy L- and P-band flight lines in the BERMS area from the CANEX 2010 campaign [Magagi  
05 2012] and the AirMOSS EV-S1 investigation [Chapin 2012, 2018] provide the potential to establish  
06 longer time series.

07  
08 Flight planning for the Canadian transects benefited tremendously from consultations with our  
09 Canadian colleagues and interested parties in Yellowknife, NT and Whitehorse, YT in 2015 and 2016.  
10 Extensive discussions with the Government of the Northwest Territories (GNWT), the Government of  
11 the Yukon Territory, First Nations representatives, and scientists from Polar Knowledge Canada  
12 (POLAR), the NWT Center for Geomatics, and the Canadian Forestry Service (CFS) Northern Forestry  
13 Centre (NoFC) were critical to designing a strategy that captured many of their observing priorities.  
14 Subsequent discussions in Yellowknife during 2017 and 2018 enabled us to disseminate preliminary  
15 results and coordinate the flights with same-day field data acquisitions.

16



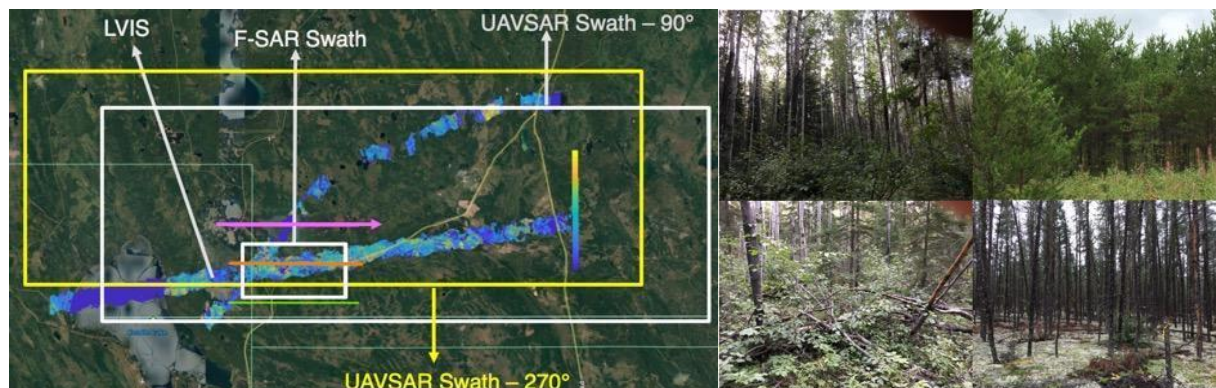
#### 17 4 TomoSAR Measurements of Boreal Forest Structure

18 SAR tomographic methods have proven extremely adept at measuring vegetation vertical structure at a  
19 variety of wavelengths including L- and P-bands. The three-dimensional vegetation structure and its  
20 changes resulting from either natural or anthropogenic causes are key ecosystem monitoring parameters.  
21 ABoVE collected tomographic L- and P-band SAR data over the boreal forest near Delta Junction, AK  
22 in September of 2017. UAVSAR (L-band) and the German Space Agency's F-SAR (L- and S-bands)  
23 acquired coordinated tomographic SAR data at the BERMS site near Saskatoon, SK in August 2018.  
24 Ground truth data sets and LiDAR data from the NASA LVIS system were also acquired at BERMS in  
25 2017 [Blair 2018]. We compared L- and P-band tomography at Delta Junction and L-band and S-band  
26 tomography from the two systems, to each other, and to the LiDAR data sets at BERMS. Here we  
27 provide a preliminary analysis of the data acquired at BERMS.

28  
29 BERMS is a southern boreal forest site with gentle topography dominated by Jack Pine and Aspen  
30 stands. There is active logging in the area and the site contains clear cut areas and new growth stands in  
31 various maturity states. The tomography data acquisition at BERMS was planned jointly in cooperation  
32 with the German Space Agency (DLR) who flew the F-SAR radar and acquired data at L-band and S-  
33 band. The UAVSAR and F-SAR flight lines were designed to overlap each other and LVIS data  
34 acquired at the site in 2017. LVIS reacquired BERMS area data again in 2019 with the LVIS-F and  
35 LVIS-C instruments [<https://lvis.gsfc.nasa.gov/Data/Maps/ABOVE2019Map.html>]. Figure 5 (left)  
36 shows swaths for the UAVSAR and F-SAR radars along with the LVIS data. UAVSAR acquired L-  
37 band tomography data on a racetrack pattern to get multiple incidence angle data for most points in the  
38 swath. Because UAVSAR and F-SAR fly at 12500 mAGL and 4200 mAGL, respectively, it is not  
39 possible to acquire data with the same incidence angles across the swath. Thus, we configured the flight  
40 lines to overlap so that the 40° incidence angle points would coincide. Figure 5 (right) shows photos  
41 collected at four of our seventeen ground truth sites during the tomoSAR acquisitions.

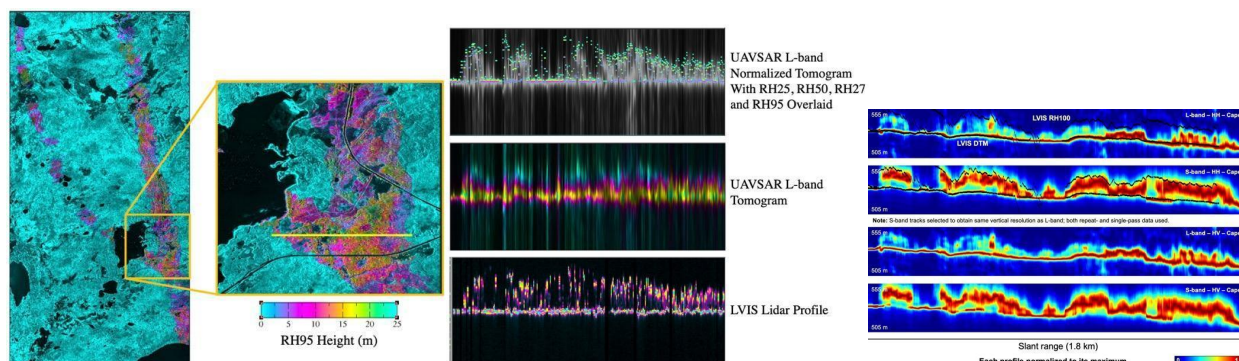
42  
43 LVIS full waveform LiDAR provides surface elevations and tree height estimates as well as LiDAR  
44 echo strength throughout the canopy and thereby information on the canopy internal structure. From  
45 LVIS waveforms many products are possible including surface elevation, tree height, moments of the  
46 returned waveform distribution and cumulative percentile elevations. We compared these waveforms to  
47 radar tomographic profiles for the different radar wavelengths.

48  
49 BERMS field measurements consist of soil moisture measurements at the 17 sites using the average of  
50 15 measurements distributed over 60 m × 60 m plots on the day of the UAVSAR radar observations. At  
51 BERMS the soil was very dry, roughly 10% volumetric soil moisture or less, during the radar  
52 observations. During the summer of 2020 diameter at breast height (DBH) measurements, used to  
53 estimate biomass, for a subset of our selected sites was planned but postponed due to COVID-19.  
54



55  
 56 **Figure 5.** LEFT: Experimental design for the BERMS area TomoSAR flights in August 2018. The large White and yellow  
 57 boxes show the ~18 km-wide UAVSAR L-band swaths. The offset is due to the off-nadir viewing angle of the L-band SAR –  
 58 it is pointed to the south when flying the 270° swath and pointed north when flying the 90° swath. The small white box near  
 59 the center of the image marks the ~3 km-wide F-SAR swath. LVIS LiDAR data are the ~1.5 km-wide colored swaths across  
 60 the image; the color scaling reflects the canopy height. RIGHT: Photos from four of the 17 plots used for in situ ground truth  
 61 measurement at BERMS. Vegetation at BERMS was mostly Jack Pine and Aspen with many areas having dense understory  
 62 vegetation. Most areas have substantial detritus and ground litter left over from previous logging operations. © Google Earth

63 **Figure 6** compares UAVSAR L-band tomography with F-SAR L-band and S-band tomography and  
 64 LVIS LiDAR data along a transect shown as a yellow line on the right in the figure. Tree height along  
 65 the transect varied from 10-20 m. Middle of Figure 2 is the UAVSAR L-band transect. Top of the figure  
 66 shows the LVIS RH25m RH50, RH75 and RH95 profiles overlaid on the UAVSAR tomogram and  
 67 below are the radar and LiDAR vertical profiles. On the left of Figure 2 are the F-SAR L-band and S-  
 68 band tomographic profiles along with the LVIS RH100 data. The L-band radar profiles exhibit power  
 69 concentrated at the base of the canopy whereas the LVIS LiDAR data show more return from the  
 70 middle portion of the canopy. S-band obtains greater returns in the upper canopy compared to L-band  
 71 and show more uniform scattering within the canopy.



73  
 74 **Figure 6.** On the left shows location of transect as yellow line overlaid on UAVSAR imagery in grayscale and LVIS RH95 data is color  
 75 where UAVSAR L-band, DLR F-SAR L and S-band and LVIS LiDAR profiles are compared. Center figure shows UAVSAR L-band  
 76 tomographic profiles along the transect along with the corresponding LVIS LiDAR profiles. On the right are the corresponding F-SAR L  
 77 and S-band tomographic profiles. The L-band radar profiles exhibit power concentrated at the base of the canopy whereas the LVIS LiDAR  
 78 data show more return from the middle portion of the canopy. S-band obtains greater returns in the upper canopy compared to L-band and  
 79 show more uniform scattering within the canopy.



## 80 5 ABoVE SAR Data Products

81 Here we highlight some data sets enabling or derived from the ABoVE L- and P-band airborne SAR  
82 acquisitions. They represent the current state of the art for the study of permafrost-affected ecosystems  
83 using SAR. The ABoVE science team continues to develop additional products and the insights from  
84 these studies will be published separately. Links to the repositories for each of these data sets are  
85 provided below.  
86

### 87 5.1 Active Layer Thickness (ALT)

88 The Permafrost Dynamics Observatory (PDO) data product estimates seasonal subsidence, active layer  
89 thickness (ALT), soil Volumetric Water Content (VWC), and uncertainties at 30-m resolution for 66  
90 flight lines across Alaska and Northwest Canada [Michaelides 2021; Chen 2021a,b]. The PDO retrieval  
91 uses L-band Synthetic Aperture Radar (SAR) data acquired by the Uninhabited Aerial Vehicle  
92 Synthetic Aperture Radar (UAVSAR) instrument and P-band data acquired by the Airborne Microwave  
93 Observatory of Subcanopy and Subsurface (AirMOSS) instrument. The PDO results for each flight line  
94 appear in separate netcdf files. Each line has a spatial resolution of 30 meters on the ABoVE common  
95 grid with a width of 22 km based on the swath width of the AirMOSS instrument. The flight lines as a  
96 whole cover many ecosystem types and provide north-south and east-west gradients in ALT and soil  
97 moisture across the ABoVE domain ([https://daac.ornl.gov/cgi-bin/dsviewer.pl?ds\\_id=1796](https://daac.ornl.gov/cgi-bin/dsviewer.pl?ds_id=1796)).

98 **Table 1** defines all variables in PDO data files. The first eight variables represent the four primary  
99 outputs of the PDO algorithm and associated uncertainties. Subsidence and ALT represent one-time  
00 measurements for the 2017 thaw season [Schaefer 2021]. VWC, defined as the ratio of water volume to  
01 total soil volume, represents soil moisture at maximum thaw for 2017. We assume a vertical profile of  
02 VWC and estimate Sw0 and wtd, the parameters that define the exact shape of the assumed profile. The  
03 product includes a Python script that will create a map of VWC averaged over any user specified depth  
04 range. We included maps of VWC averaged over depth ranges of hand-held soil moisture probes  
05 commonly used in ABoVE fieldwork.

06  
07 **Table 1. Variables in the Permafrost Dynamics Observatory (PDO) data files**

Variable	Full Name	Units	Description
alt	Active Layer Thickness	M	Maximum thaw depth at the end of summer
sub	Subsidence	M	Surface subsidence from start of thaw after snow melt to maximum thaw depth in August or September
Sw0	Surface Saturation Fraction	m <sup>3</sup> /m <sup>3</sup>	The ratio of water volume to pore space volume at the surface or zero meters depth
wtd	Water Table Depth	M	The depth from the surface to the level where the soil is 100% saturated
alt_unc	Uncertainty ALT	M	Uncertainty of estimated ALT



sub_unc	Uncertainty Subsidence	M	Uncertainty of estimated seasonal subsidence
Sw0_unc	Uncertainty Surface Saturation Fraction	m <sup>3</sup> /m <sup>3</sup>	Uncertainty of estimated surface water saturation fraction
wtd_unc	Uncertainty Water Table Depth	M	Uncertainty of estimated water table depth
mv_6cm	VWC from 0 to 6 cm	m <sup>3</sup> /m <sup>3</sup>	The ratio of water volume to soil volume averaged over zero to 6 cm depths
mv_12cm	VWC from 0 to 12 cm	m <sup>3</sup> /m <sup>3</sup>	The ratio of water volume to soil volume averaged over zero to 12 cm depths
mv_20cm	VWC from 0 to 20 cm	m <sup>3</sup> /m <sup>3</sup>	The ratio of water volume to soil volume averaged over zero to 20 cm depths
mv_alt	VWC from 0 to ALT	m <sup>3</sup> /m <sup>3</sup>	The ratio of water volume to soil volume averaged over the entire active layer, from zero to ALT

08 **5.2 Alaska Active Layer and Soil Moisture Properties from Airborne P-band SAR**

09 Chen et al. [2019b] synthesized the P-band polarimetric synthetic aperture radar (PolSAR) data  
 10 collected in August and October of 2014 and 2015 during the AirMOSS EV-S1 investigation with the  
 11 ABoVE P-band measurements collected in August and October of 2017 to estimate soil geophysical  
 12 properties over 12 study sites in Northern Alaska (see Figure S2). Soil properties reported include the  
 13 ALT, soil dielectric constant, soil moisture profile, surface roughness, and their respective uncertainty  
 14 estimates at 30-m spatial resolution (<https://doi.org/10.3334/ORNLDAAAC/1657>).

15  
 16 Most of the study sites are located within the continuous permafrost zone and where the aboveground  
 17 vegetation consisting mainly of dwarf shrub and tussock/sedge/moss tundra has a minimal impact on P-  
 18 band radar backscatter. These data were used as inputs to the L-band ReSALT data described in Section  
 19 5.1.

20 **5.3 In Situ Soil Moisture and Thaw Depth Measurements**

21 In situ measurements of soil moisture, thaw depth, and other quantities are essential to calibrate and  
 22 validate ABoVE SAR retrievals. The ABoVE team established a set of standardized measurement  
 23 protocols for field plots to ensure uniform data products and quality in measurements collected by  
 24 different groups across the ABoVE domain and across multiple years. Numerous teams collected in situ  
 25 data during the initial 2017 Airborne Campaign, with more targeted field acquisitions conducted in  
 26 2018 and 2019 [Bourgeau-Chavez et al. 2019a,b, 2021; Bakian-Dogaheh 2020; Loboda 2021].

27  
 28 Bourgeau-Chavez and coworkers [2019a,b; 2021] collected soil moisture at 6, 12, 20, and 50 cm depths,  
 29 ALT, soil profiles and biophysical measurements of aboveground canopy and ground layers in the  
 30 Greater Slave Lake Region (C4). These data provide vegetation community characteristics and  
 31 biophysical data collected in 2018 from areas that were burned by wildfire in 2014 and 2015, and from  
 32 nine unburned validation sites. Vegetation data include vegetation inventories, ground cover, regrowth,



33 tree diameter and height, and woody seedling/sprouting data at burned sites, and similar vegetation  
34 community characterization at unburned validation sites. Additional measurements included soil  
35 moisture, collected for validation of the UAVSAR airborne collection, and depth to frozen ground at the  
36 nine unburned sites. This 2018 fieldwork completes four years of field sampling at the wildfire areas.  
37

38 Bakian-Dogaheh et al. [2020] measurements included soil dielectric properties, temperature, and  
39 moisture profiles, active layer thickness (ALT), and measurements of soil organic matter, bulk density,  
40 porosity, texture, and coarse root biomass from the surface to permafrost table in soil pits at selected  
41 sites along the Dalton Highway in Northern Alaska (A1). Their investigation sites included Franklin  
42 Bluffs, Sagwon, Happy Valley, Ice Cut, and Imnavait Creek. Measurements collected at Franklin Bluffs  
43 were concurrent with an August 2018 ABoVE L-band flight.  
44 (<https://doi.org/10.3334/ORNLDAAAC/1759>).  
45

46 Loboda et al [2022] collected field measurements from unburned sites and single and repeated burns in  
47 the Noatak River valley and the Seward Peninsula regions of the Alaska tundra in July-August in the  
48 years 2016-2018. The data include ocular assessment of vegetation cover, soil moisture at 6 and 12 cm,  
49 soil temperature at 10 cm, organic soil thickness, thaw depth, and weather measurements.  
50 (<https://doi.org/10.3334/ORNLDAAAC/1919>)  
51

52 The strong partnership between the ABoVE and NGEE-Arctic projects also resulted in coordinated  
53 same-day acquisition of airborne L- and P-band SAR data with in situ soil moisture and thaw depth  
54 measurements over the NGEE-Arctic study site at Barrow (Utqiagvik), AK and the Seward Peninsula  
55 watersheds near Teller, AK, Council, AK, and Kougarak, AK [Wilson 2018]. These data provide  
56 critical calibration for the ABoVE SAR retrievals under continuous (Utqiagvik) and discontinuous  
57 (Seward Peninsula) permafrost conditions. Version 2 (V2) of the in situ soil moisture and thaw depth  
58 measurements covering years 2017-2019 was released in November 2020.  
59 (<https://doi.org/10.5440/1423892>)

## 60 **6 Synergy with Other Airborne Sensors**

61 Miller et al. [2019] described the overall ABoVE Airborne Campaign design strategy and anticipated  
62 airborne sensor synergies. Here, we highlight three SARs and a LiDAR – AirSWOT (NASA), F-SAR  
63 (DLR), LS-ASAR (ISRO) and LVIS (NASA) – whose acquisitions in the ABoVE domain were  
64 specifically designed to complement and leverage the ABoVE L- and/or P-band SAR acquisitions.  
65 Many other airborne sensor synergies are being exploited by the ABoVE science team and are reported  
66 separately.

### 67 **6.1 AirSWOT**

68 NASA's AirSWOT airborne instrument suite has been developed to support the Surface Water and  
69 Ocean Topography (SWOT) mission. The heart of AirSWOT is the Ka-band SWOT Phenomenology  
70 Airborne Radar (KaSPAR). KaSPAR collects two swaths of across-track interferometry data: one swath



71 from nadir to 1 km and a second swath that extends from 1 km to 5 km off-nadir. AirSWOT flight lines  
72 for ABoVE were designed to center the AirSWOT swath on the center of the P-band swath for  
73 maximum overlap. KaSPAR is complemented by a high-resolution color-infrared (CIR) Digital Camera  
74 System [Kyzivat 2019a,b] and a Precision Inertial Measurement Unit (IMU) for accurate attitude and  
75 positioning information. In 2015 AirSWOT made pre-ABoVE deployments to the Tanana River Valley  
76 [Altenau 2017] and the Yukon Flats [Pitcher 2019a, 2019b] in Region A3.

77  
78 In 2017, AirSWOT deployed to acquire  
79 early season (May-June) and late season  
80 (August) WSEs across the ABoVE  
81 domain. **Figure 7** shows the concentration  
82 of AirSWOT lines in wetlands complexes  
83 in the boreal forest, across the Canadian  
84 Shield, along the Mackenzie River Valley,  
85 and into the Arctic tundra. All of these  
86 regions contain overlapping L- and P-  
87 band acquisitions. Of special interest are  
88 the lines in the Peace-Athabasca Delta  
89 (36000: PADeE and 18035: PADeW)  
90 and the Yukon Flats (21508: YFlatW,  
91 21609: YflatE, and 04707: FtYuko) and  
92 Trail Valley Creek, NT (01703: TukHwy)  
93 where extensive on-water measurements  
94 were made [Pitcher 2020]. Future joint  
95 analyses of the Ka- and L-band data will  
96 highlight the advances possible in pan-  
97 Arctic hydrology from the upcoming NISAR and SWOT missions.

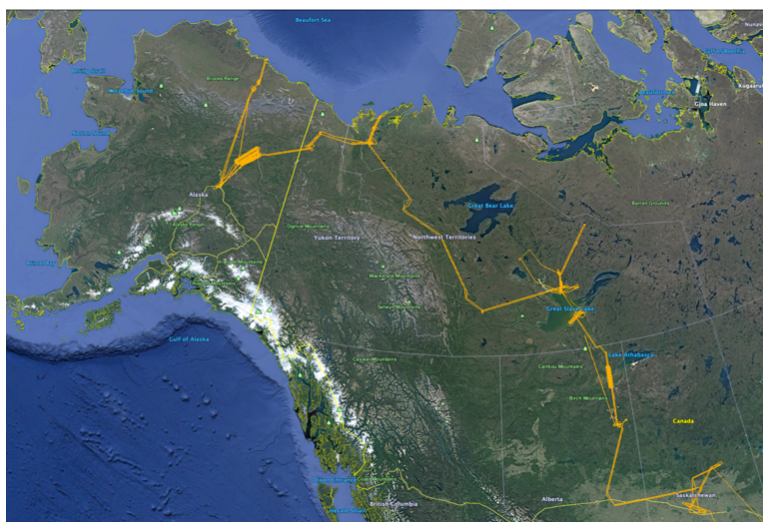


**Figure 7.** AirSWOT flight lines acquired during the 2017 ABoVE airborne campaign sampled wetlands ranging from the Arctic Ocean coast to the southern boreal forest. AirSWOT's Ka-band acquisitions were designed to overlap with the L- and P-band SAR near-field acquisitions (See Fig. 1). © Google Earth

98  
99  
00  
01  
02  
03  
04  
05  
06  
07  
08  
09  
10





## 11 6.2 F-SAR

12 The German Space Agency (DLR) developed  
13 the F-SAR instrument as an advanced  
14 airborne SAR testbed for technology and  
15 remote sensing applications [Reigber 2013].  
16 F-SAR operates fully polarimetric at X-, C-,  
17 S-, L- and P-bands and features single-pass  
18 polarimetric interferometric SAR (PolInSAR)  
19 capabilities in X- and S-bands [Reigber  
20 2013]. The radar covers an off-nadir angle  
21 range of 25 to 60 degrees and provides sub-  
22 meter scale spatial resolution from flight  
23 altitudes up to 6000 mAGL.

24  
25 During August 2018 and April 2019, F-SAR  
26 was deployed to northern Canada as part of  
27 DLR's permafrost airborne SAR experiment  
28 (PerMASAR). It was configured in X-, C-, S-  
29 and L-band mode and flew onboard a Dornier  
30 Do 228-212 research aircraft. Measurements  
31 were acquired from ~4500 mAGL.  
32 Coordinated tomoSAR transects were flown  
33 over the BERMS site in the southern boreal  
34 forest on 18 August (UAVSAR) and 23  
35 August (F-SAR). Preliminary results [Hensley  
36 2020] are summarized in Section 6. F-SAR  
37 also acquired data over the Scotty Creek  
38 watershed, flux towers, and AOIs (Figure 8),  
39 the Smith Creek flux tower (Wrigley, NT),  
40 Baker Lake, Havipak Creek, Trail Valley  
41 Creek, and Herschel Island, providing  
42 extensive opportunities to cross-compare F-  
43 SAR and the ABoVE SAR acquisitions.

44  
45

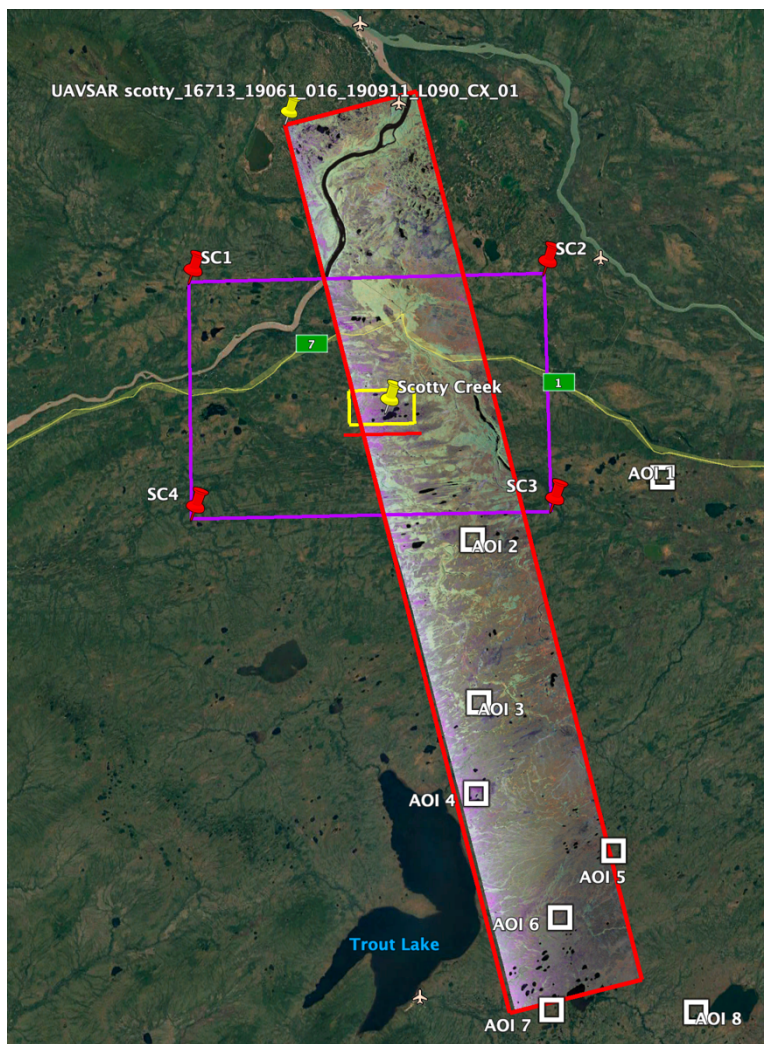


**Figure 8.** Overlap of the F-SAR acquisition at Scotty Creek, NT (yellow box) and the ABoVE L-band SAR line 16713 (red box & polarized SAR false color). The ABoVE line also captures Scotty Creek AOIs 2 – 6 (see Region C3 details, Sec. 5.3). The SAR data will complement and benefit from the extensive ground-based data acquired in this area [Quinton 2019]. © Google Earth



### 46 6.3 LS-ASAR (ISRO)

47 The Indian Space Research Organisation (ISRO)  
48 and NASA are jointly developing the NASA-  
49 ISRO Synthetic Aperture Radar (NISAR), which  
50 will map Earth's surface in L-band and S-band  
51 every 12 days [Rosen 2017]. As a precursor to the  
52 NISAR mission, ISRO has developed a L- and S-  
53 Band-Airborne SAR (LS-ASAR) to prepare the  
54 community to maximize the scientific and  
55 societal benefits of NISAR data [Ramanujam  
56 2016; 2019; Mehra 2019]. LS-ASAR operates in  
57 Dual, Quad, and Hybrid and Polarization modes  
58 in both L- and S-bands. It covers incidence angles  
59 from 24°-77° with swaths ranging from 5.5 km to  
60 15 km.

61  
62 In December 2019 LS-ASAR flew a series of  
63 Arctic sea ice sorties from Fairbanks, AK. During  
64 this deployment, LS-ASAR also acquired data  
65 over a number of the ABoVE flight lines in  
66 Regions A1 (North Slope) and A3 (Eastern  
67 Interior) as well as over a number of glacier sites  
68 in the Alaska Range. The acquisitions are  
69 available via the NASA & ISRO ASAR  
70 Campaign page ([https://uavsar.jpl.nasa.gov/cgi-  
71 bin/deployment.pl?id=L20191101](https://uavsar.jpl.nasa.gov/cgi-bin/deployment.pl?id=L20191101)) and are summarized in Figure 9. These data provide snow-on  
72 coverage that was a known deficiency of previous ABoVE airborne campaigns. Additionally, the LS-  
73 ASAR data extend coverage of these regions to S-band.  
74

### 75 6.4 LVIS

76 The Land, Vegetation, and Ice Sensor (LVIS) is an airborne, full waveform scanning laser altimeter  
77 which produces topographic maps with decimeter accuracy as well as vegetation vertical height and  
78 structure measurements [Blair 1999a,b]. Flight lines for LVIS (~1.4 km swath) were slaved to the  
79 centerline of the P-band swath during ABoVE, except where deviations were required to capture critical  
80 ground sites. LVIS-C (classic configuration) was deployed in 2017 aboard a B-200 and achieved limited  
81 coverage (Figure 10, left panel). During 2019, the new LVIS Facility instrument (LVIS-F) as well as  
82 LVIS-C were deployed on the NASA Gulfstream-V and achieved coverage of all legacy SAR lines  
83 (Figure 10, right panel).  
84

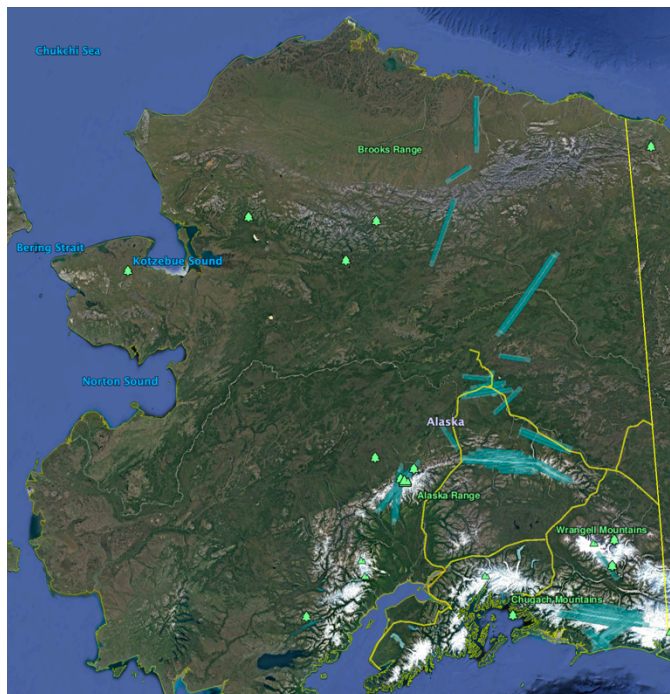


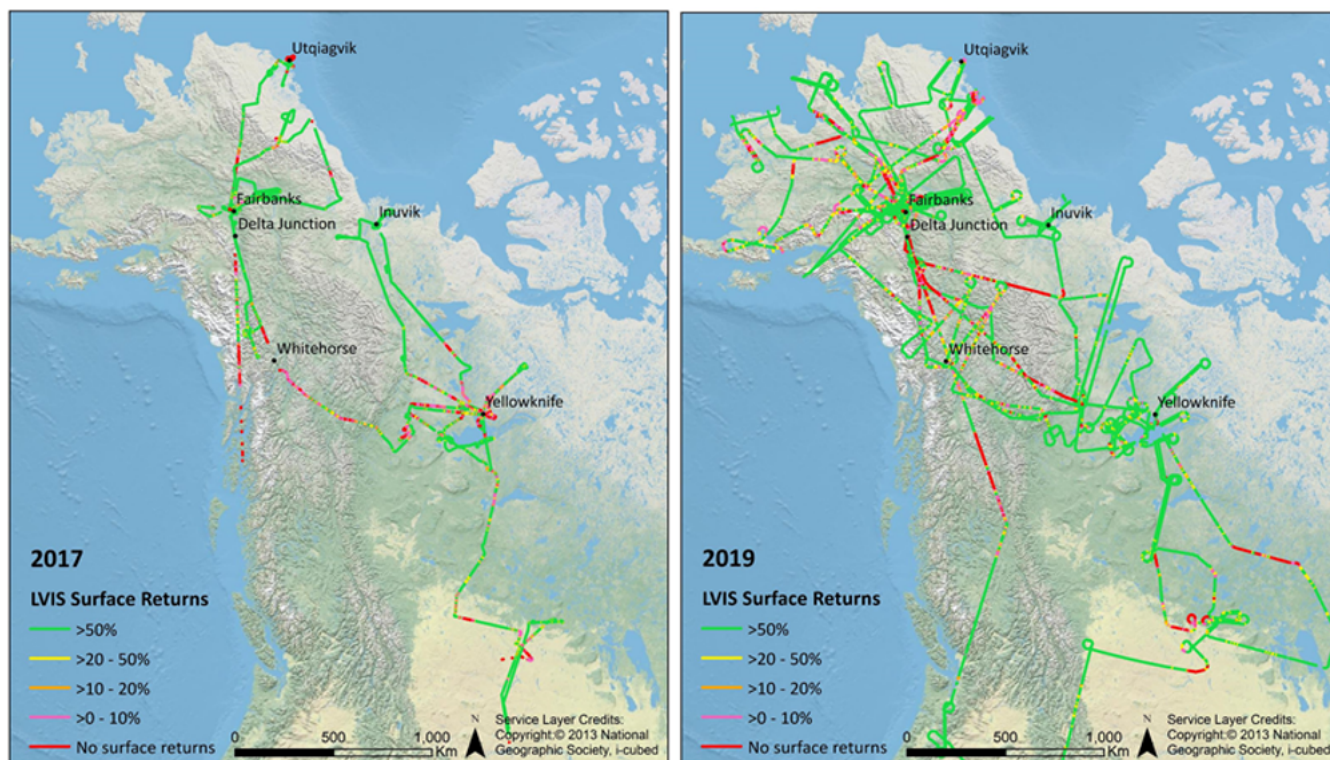
Figure 9. L- and S-band SAR lines acquired over Alaska during the December 2019 ASAR Campaign. ASAR flight lines on the North Slope, in the Yukon Flats, and in the Western Interior exactly overlap ABoVE flight lines. These early winter acquisitions provide a preliminary look at cold season SAR data that will be explored in greater detail in the planned ABoVE-SnowEx campaign. © Google Earth



85 LVIS' unique capability for measuring the sub-meter topography beneath boreal forest canopies  
86 complemented the tomoSAR acquisitions over Delta Junction, AK and the BERMS site in northern  
87 Saskatchewan [Hensley 2020; Section 6]. LVIS altimetry will also prove valuable in analyses of such  
88 variables as permafrost degradation, active layer thickness, and water surface elevation; however,  
89 LVIS' significantly narrower swath limits the spatial extent over which these analyses may be  
90 performed.

91  
92 In June-July 2017, the NASA LVIS Facility was deployed to sites in northern Canada and Alaska as  
93 part of NASA's Arctic-Boreal Vulnerability Experiment (ABoVE) 2017 airborne campaign. During the  
94 4-week deployment of LVIS-F, a total of 15 flights were flown over diverse science targets based out of  
95 multiple airports in Canada and Alaska. Data are available in both Level1B and Level2 formats (**Table**  
96 **2**). The Level1b data files contain the geolocated laser waveform data for each laser footprint. The  
97 Level2 data files contain canopy top and ground elevations and relative heights derived from the  
98 Level1b data. ABoVE LVIS L1B Geolocated Return Energy Waveforms, Version 1 [Blair and Hofton,  
99 2018a] and L2 Geolocated Surface Elevation Product, Version 1 [Blair and Hofton, 2018b] may be  
00 obtained from the National Snow and Ice Data Center via <https://doi.org/10.5067/UMRAWS57QAFU>  
01 and <https://doi.org/10.5067/IA5WAX7K3YGY>, respectively.

02



03  
04 **Figure 10. Flight lines for the LVIS 2017 flights (left) and 2019 flights (right) were designed to overlap with the near-filed portions**  
05 **of the L-band and P-band SAR swaths to maximize opportunities for synergistic science. Aircraft and weather limited coverage**  
06 **during the 2017 campaign, but complete coverage of the SAR flight lines was achieved in 2019. These data will enable studies of**  
07 **SAR/LiDAR fusion over the Arctic-boreal regions as a precursor to NISAR/IceSat-2 studies. © National Geographic Society**



08

09 **Table 2. 2017 LVIS Data Products**

<b>LVIS Data Products</b>	<b>Format</b>
Flight Trajectories	KMZ
Camera Trajectories	KMZ
LVIS L1A Camera Imagery	JPG*
LVIS L1B Geolocated Waveforms	HDF, LDS 2.0.2
LVIS L2 Elevation and Height Products	ASCII TXT, LDS 2.0.2a

10

11 In July-August 2019, the NASA LVIS Facility and LVIS Classic were deployed to sites in northern  
12 Canada and Alaska as part of NASA's ABoVE 2019 airborne campaign. The increased range and  
13 endurance of the Gulfstream-V platform enabled extensive sampling, including: all L-band SAR lines,  
14 multiple IceSAT-2 underflights, and numerous ABoVE field sites. The available data products are given  
15 in **Table 3**.

16

17 **Table 3. 2019 LVIS Data Products**

<b>LVIS Data Products</b>	<b>Format</b>
Flight Trajectories	KMZ
Coverage Maps	KMZ
LVIS Classic L1B Geolocated Waveforms	HDF, LDS 2.0.3
LVIS Classic L2 Elevation and Height Products	ASCII TXT, LDS 2.0.3
LVIS Facility L1B Geolocated Waveforms	HDF, LDS 2.0.3
LVIS Facility L2 Elevation and Height Products	ASCII TXT, LDS 2.0.3

## 18 **6.5 G-LiHT**

19 Zhao et al. [2022] used ABoVE airborne L- and P-band SAR to map boreal forest species and canopy  
20 height in the Tanana Valley State Forest (TVSF) near Delta Junction, AK. They employed Random  
21 Forests to train separate regression models for canopy height mapping and a classification model for  
22 forest species mapping. Data derived from NASA's Goddard LiDAR, Hyperspectral, and Thermal  
23 Imager (G-LiHT) system [Cook 2013] were treated as ground truth for the canopy height model  
24 (CHM). Forest species prediction were referenced against (TVSF) Timber Inventory and Forest  
25 Inventory and Analysis (FIA) data. The experimental results show the proposed method yields a root-  
26 mean-square error of 1.90 m for forest height estimation and overall accuracy of 79.5% for forest  
27 species classification. A significant finding was that PolSAR decomposition parameters, such as volume  
28 scattering and entropy, strongly influenced the canopy height estimates. Interestingly, topography  
29 played a crucial role in the species classification.

30

31

32



## 33 7 Data Availability

34  
35 Links to the ABoVE L- and P-band SAR products, supporting data, derived products, and ancillary  
36 measurements are provided in the Appendix. Formal citations to all DOIs are provided in the  
37 References. The L- and P-band SAR data may be found at the JPL UAVSAR data portal,  
38 <https://uavsar.jpl.nasa.gov/cgi-bin/data.pl>. L-band data may also be accessed via the UAVSAR portal at  
39 the Alaska SAR Facility (ASF) DAAC (<https://asf.alaska.edu/data-sets/sar-data-sets/uavsar/>) while  
40 AirMOSS P-band data may be accessed via the ORNL DAAC, [https://daac.ornl.gov/get\\_data/#projects](https://daac.ornl.gov/get_data/#projects),  
41 select “AirMOSS”.

42  
43 Miller et al. [2023; <https://doi.org/10.3334/ORNLDAAAC/2150>] provides a detailed description of all 80  
44 SAR flight lines and how each fits into the ABoVE experimental design. Extensive maps, tables, and  
45 hyperlinks give direct access to every flight plan as well as individual flight lines. It is a guide to enable  
46 interested readers to fully explore the ABoVE L- and P-band SAR data.

## 49 8 Summary

50 The ABoVE project conducted airborne L-band PolInSAR surveys in 2017, 2018, 2019 and 2022 across  
51 Alaska and northwestern Canada. These were complemented by a P-band PolInSAR survey in 2017  
52 along the same transects. This time series provides a powerful data set with which to evaluate the state  
53 of permafrost, active layer thickness, soil moisture, boreal forest structure, above ground biomass, and  
54 water surface elevation. Additional studies leverage the PolInSAR data to address fire disturbance and  
55 recovery, thermokarst feature development, and retrogressive permafrost thaw megaslumps. Many of  
56 these analyses are in progress and will be published separately.

57  
58 Miller et al. [2023] provides extensive, fully hyperlinked notes on the airborne SAR data. Researchers  
59 may discover these data via daily sorties and/or individual flight lines. Alternatively, they may be  
60 explored via the interactive map at the JPL UAVSAR data portal, ([https://uavsar.jpl.nasa.gov/cgi-  
61 bin/data.pl](https://uavsar.jpl.nasa.gov/cgi-bin/data.pl)) which provides links to the individual flight line data, maps, and related flight plans that  
62 acquired data over one or more of the individual flight lines. We have also identified the ground-based  
63 anchor points for each flight line to facilitate comparisons with those data. Calibration and validation  
64 data sets as well as many derived products produced by the ABoVE Science Team may be found at the  
65 Arctic Boreal Vulnerability Experiment (ABoVE) landing page at the ORNL DAAC  
66 ([https://daac.ornl.gov/cgi-bin/dataset\\_lister.pl?p=34](https://daac.ornl.gov/cgi-bin/dataset_lister.pl?p=34)).

67  
68 The example studies (Sections 4 and 5) and multi-instrument synergies (Section 6) described here are  
69 only a small portion of the studies currently being undertaken by the ABoVE Science Team and the  
70 SAR Working Group. We anticipate many new and innovative uses of the L-band and P-band SAR data  
71 as the ABoVE team expands its range of synthesis activities in Phase 3.



72  
73 The ABoVE L-band SAR flights planned for 2020 and 2021 were postponed due to the global COVID-  
74 19 pandemic and safety considerations; however, flights were resumed in 2022 and we anticipate at  
75 least one more thaw season campaign in 2024. Finally, we note that the data and analyses discussed  
76 here set the stage for the upcoming NISAR mission (expected launch in 2023). NISAR will deliver  
77 global L- and S-band imagery with a 12-day revisit. Its emphasis on snow- and ice-covered surfaces has  
78 obvious applications in the ABoVE domain, and its global coverage will allow researchers to test the  
79 methods developed for the ABoVE domain across the pan-Arctic. Beyond NISAR, NASA is studying  
80 architectures for the Surface Deformation and Change (SDC) Earth System Observatory Mission and  
81 ESA are developing the Rose-L Copernicus expansion mission. SDC and Rose-L are also envisioned as  
82 an L-band sensors. NISAR, SDC, and Rose-L will all benefit from the ABoVE SAR studies,  
83 algorithmic advances, and lessons learned.

#### 84 **9 Supplemental Information**

85 Supplemental Information on the Legacy L-band and P-band flight lines as well as the P-band flight  
86 lines acquired during the ABoVE campaign are provided separately.

#### 87 **10 Author Contributions**

88 SJG, CEM, PCG and the ABoVE Science Definition Team developed the preliminary ABoVE  
89 Implementation Plan; this was updated by SJG, CEM, PCG and the ABoVE Science Team. CEM, PCG,  
90 and EH developed the initial flight lines based on the ABoVE Implementation Plan and consultations  
91 with the ABoVE Science and partners. NSP translated the notional flight lines into the UAVSAR  
92 planning system. NSP, YL, MM, PCG, , ELH, and CEM served as Scientist on Board during the data  
93 acquisition flights. YL, SH, BC, NP and the JPL Sub-orbital Radar Science and Engineering Team  
94 (334F) processed the L- and P-band SAR data. CW, KS, MT, JB, LBC, RHC, MM, SW, MM, RJM,  
95 TL, LJ, PS AT, and RD collected cal/val field data. CW and SW coordinated ground cal/val data  
96 acquisitions at the NGEE-Arctic sites. SH, PS, NSP performed the tomoSAR analyses and SH  
97 contributed the text and images for Section 6. KS, MM and the ABoVE SAR Working Group calibrated  
98 the L-band SAR data. MM, AT, RHC processed the P-band data. NSP and YL coordinated the LS-  
99 ASAR flights and the joint BERMS area tomoSAR flights with F-SAR. DS coordinated all data product  
00 submissions to the ORNL DAAC. CEM wrote the initial manuscript and all co-authors contributed to  
01 the final version.

#### 02 **11 Competing Interests**

03 The authors declare that they have no conflict of interest



## 04 12 Acknowledgments

05 The L- and P-band SAR data acquisitions would not have been possible without the indefatigable  
06 support of our NASA pilots and flight crews. We thank John McGrath and the NASA AFRC C-20  
07 (N30502) team as well as Derek Rutovic and the NASA JSC G-III (N995NA) team. We also thank the  
08 instrument scientists, operators, and data processing team from the JPL Suborbital Radar Science and  
09 Engineering Team (334F) who were essential to the successful execution of these experiments and rapid  
10 processing of the resulting data products. The field work supporting the SAR campaigns was made  
11 possible by the excellent support from Dan Hodkinson, Sarah Sackett, and the ABoVE Logistics Office.  
12 Finally, we thank the data curation team at the Oak Ridge Distributed Active Archive Center for their  
13 support and expert advice.

14  
15 This work was supported by the NASA Terrestrial Ecology Program's Arctic-Boreal Vulnerability  
16 Experiment (ABoVE). A portion of this work was performed at the Jet Propulsion Laboratory,  
17 California Institute of Technology, under contract with National Aeronautics and Space Administration  
18 (80NM0018D0004). Government funding acknowledged.  
19

## 20 References

- 21 Abe, T., Iwahana, G., Efremov, P. V., Desyatkin, A. R., Kawamura, T., Fedorov, A., Zhegusov, Y., Yanagiya,  
22 K., and Tadono, T.: Surface displacement revealed by L-band InSAR analysis in the Mayya area, Central  
23 Yakutia, underlain by continuous permafrost, *Earth Planets Space*, 72, 138, [https://doi.org/10.1186/s40623-](https://doi.org/10.1186/s40623-020-01266-3)  
24 020-01266-3, 2020.
- 25 Airborne Imaging: Final LiDAR processing & vertical accuracy report: Prepared for the U.S. Fish and Wildlife  
26 Service, in: *LiDAR Imagery & DEM Model for Yukon Delta National Wildlife Refuge—Near Angyaravak*  
27 *Bay, Alaska*, Airborne Imaging, Calgary, AB, Canada, 28, 2011.
- 28 Allen, B. D., Braun, S. A., Crawford, J. H., Jensen, E. J., Miller, C. E., Moghaddam, M., and Maring, H.:  
29 Proposed investigations from NASA's Earth Venture-1 (EV-1) airborne science selections, in: 2010 IEEE  
30 International Geoscience and Remote Sensing Symposium, 2010 IEEE International Geoscience and Remote  
31 Sensing Symposium, 2575–2578, <https://doi.org/10.1109/IGARSS.2010.5651920>, 2010.
- 32 Alonzo, M., Dial, R. J., Schulz, B. K., Andersen, H.-E., Lewis-Clark, E., Cook, B. D., and Morton, D. C.:  
33 Mapping tall shrub biomass in Alaska at landscape scale using structure-from-motion photogrammetry and  
34 lidar, *Remote Sens. Environ.*, 245, 111841, <https://doi.org/10.1016/j.rse.2020.111841>, 2020.
- 35 Altenau, E. H., Pavelsky, T. M., Moller, D., Lion, C., Pitcher, L. H., Allen, G. H., Bates, P. D., Calmant, S.,  
36 Durand, M., and Smith, L. C.: AirSWOT measurements of river water surface elevation and slope: Tanana  
37 River, AK, *Geophys. Res. Lett.*, 44, 181–189, <https://doi.org/10.1002/2016GL071577>, 2017.
- 38 Kenaston / Brightwater Creek Mesonet Site, SK - CCRNetwork:  
39 <http://www.ccrnetwork.ca/science/WECC/prairie/brightwater-creek.php>, last access: 30 April 2021.
- 40 Bakian-Dogaheh, K., Chen, R. H., Moghaddam, M., and Tabatabaenejad, A.: Electromagnetic scattering  
41 behavior of a new organic soil dielectric model for long-wavelength radar retrieval of permafrost active layer  
42 soil properties, 2020 IEEE International Geoscience and Remote Sensing Symposium, 2020.



- 43 Bakian-Dogaheh, K., R.H. Chen, M. Moghaddam, Y. Yi, and A. Tabatabaenejad. 2020. ABoVE:  
44 Active Layer Soil Characterization of Permafrost Sites, Northern Alaska, 2018. ORNL DAAC, Oak  
45 Ridge, Tennessee, USA. <https://doi.org/10.3334/ORNLDAAAC/1759>
- 46 Banks, S. N., Ullmann, T., Duffe, J., Roth, A., King, D., Demers, A.-M., Hogg, A., Schmitt, A., Baumhauer, R.,  
47 and Dech, S.: Multi-frequency analysis of high resolution quad-pol Radarsat-2 and dual-pol TerraSAR-X  
48 data for land cover classification in Arctic Coastal Ecosystems, Mackenzie Delta, beaufort sea, 3548–3551,  
49 <https://doi.org/10.1109/IGARSS.2012.6350653>, 2012.
- 50 Banks, S. N., King, D. J., Merzouki, A., and Duffe, J.: Characterizing Scattering Behaviour and Assessing  
51 Potential for Classification of Arctic Shore and Near-Shore Land Covers with Fine Quad-Pol RADARSAT-2  
52 Data, *Can. J. Remote Sens.*, 40, 291–314, <https://doi.org/10.1080/07038992.2014.979487>, 2014.
- 53 Barr, A. G., Morgenstern, K., Black, T. A., McCaughey, J. H., and Nesic, Z.: Surface energy balance closure by  
54 the eddy-covariance method above three boreal forest stands and implications for the measurement of the  
55 CO<sub>2</sub> flux, *Agric. For. Meteorol.*, 140, 322–337, <https://doi.org/10.1016/j.agrformet.2006.08.007>, 2006.
- 56 Bennett, A. J., Thompson, W. L., and Mortenson, D. C.: Vital Signs Monitoring Plan Southwest Alaska Network:  
57 Inventory and Monitoring Program, Natl. Park Serv., 2006.
- 58 Blair, J. B and Hofton, M.: ABoVE LVIS L2 Geolocated Surface Elevation Product, Version 1,  
59 <https://doi.org/10.5067/IA5WAX7K3YGY>, 2018.
- 60 Blomberg, E., Ulander, L. M. H., Tebaldini, S., and Ferro-Famil, L.: Evaluating P-Band TomoSAR for Biomass  
61 Retrieval in Boreal Forest, *IEEE Trans. Geosci. Remote Sens.*, 59, 3793–3804,  
62 <https://doi.org/10.1109/TGRS.2020.3020775>, 2021.
- 63 Bourgeau-Chavez, L. L., French, N. H. F., Grelick, S. E., Jenkins, L., Battaglia, M., Serocki, E., and Billmire, M.:  
64 ABoVE: Burn Severity, Fire Progression, Landcover and Field Data, NWT, Canada, 2014, ORNL DAAC,  
65 <https://doi.org/10.3334/ORNLDAAAC/1307>, 2016.
- 66 Bourgeau-Chavez, L. L., Grelick, S. E., Jenkins, L., Battaglia, M., Serocki, E., and Billmire, M.: ABoVE: Burn  
67 Severity, Fire Progression, and Field Data, NWT, Canada, 2015-2016, ORNL DAAC,  
68 <https://doi.org/10.3334/ORNLDAAAC/1548>, 2017.
- 69 Bourgeau-Chavez, L. L., Graham, J. A., Grelick, S. E., French, N. H. F., Battaglia, M., Hansen, D., and Tanzer,  
70 D.: ABoVE: Ecosystem Map, Great Slave Lake Area, Northwest Territories, Canada, 1997-2011, ORNL  
71 DAAC, <https://doi.org/10.3334/ORNLDAAAC/1695>, 2019a.
- 72 Bourgeau-Chavez, L. L., Battaglia, M., Kane, E. S., Cohen, L. M., and Tanzer, D.: ABoVE: Post-Fire and  
73 Unburned Vegetation Community and Field Data, NWT, Canada, 2018, ORNL DAAC,  
74 <https://doi.org/10.3334/ORNLDAAAC/1703>, 2019b.
- 75 Burns, L. E., Fugro Airborne Survey Corp., and Stevens Exploration Management Corp.: Final processed  
76 database for the airborne geophysical surveys of the Alaska Highway corridor, east-central Alaska: Alaska  
77 Division of Geological & Geophysical Surveys Geophysical Report 2006-8, 1 DVD.,  
78 <https://doi.org/10.14509/17761>, 2008.
- 79 Campbell, E. M., Antos, J. A., and vanAkker, L.: Resilience of southern Yukon boreal forests to spruce beetle  
80 outbreaks, *For. Ecol. Manag.*, 433, 52–63, <https://doi.org/10.1016/j.foreco.2018.10.037>, 2019.
- 81 Chapin, E., Chau, A., Chen, J., Heavey, B., Hensley, S., Lou, Y., Machuzak, R., and Moghaddam, M.: AirMOSS:  
82 An Airborne P-band SAR to measure root-zone soil moisture, in: 2012 IEEE Radar Conference, 2012 IEEE  
83 Radar Conference, 0693–0698, <https://doi.org/10.1109/RADAR.2012.6212227>, 2012.
- 84 Chapin, E., Flores, S., Harcke, L., Hawkins, B. P., Hensley, S., Michel, T. R., Muellerschoen, R. J., Shimada, J.  
85 G., Tung, W. W., and Veeramachaneni, C.: AirMOSS: L1 S-0 Polarimetric Data from AirMOSS P-band  
86 SAR, BERMS, Canada, 2012-2015, ORNL DAAC, <https://doi.org/10.3334/ORNLDAAAC/1406>, 2018.





- 87 Chen, A. C., Parsekian, A. D., Schaefer, K., Jafarov, E. E., Panda, S. K., Liu, L., Zhang, T., and Zebker, H. A.:  
88 Pre-ABoVE: Ground-penetrating Radar Measurements of ALT on the Alaska North Slope, ORNL DAAC,  
89 <https://doi.org/10.3334/ORNLDAAC/1265>, 2015.
- 90 Chen, R. H., Tabatabaenejad, A., and Moghaddam, M.: A time-series active layer thickness retrieval algorithm  
91 using P- and L-band SAR observations, 2016 IEEE International Geoscience and Remote Sensing  
92 Symposium (IGARSS), 3672–3675, <https://doi.org/10.1109/IGARSS.2016.7729951>, 2016.
- 93 Chen, R. H., Tabatabaenejad, A., and Moghaddam, M.: Retrieval of permafrost active layer properties using P-  
94 band airmoss and L-band UAVSAR data, 2017 IEEE International Geoscience and Remote Sensing  
95 Symposium (IGARSS), 1415–1418, <https://doi.org/10.1109/IGARSS.2017.8127230>, 2017.
- 96 Chen, R. H., Tabatabaenejad, A., and Moghaddam, M.: P-Band Radar Retrieval of Permafrost Active Layer  
97 Properties: Time-Series Approach and Validation with In-Situ Observations, IGARSS 2018 - 2018 IEEE  
98 International Geoscience and Remote Sensing Symposium, 6777–6779,  
99 <https://doi.org/10.1109/IGARSS.2018.8518179>, 2018.
- 00 Chen, R. H., Tabatabaenejad, A., and Moghaddam, M.: ABoVE: Active Layer and Soil Moisture Properties  
01 from AirMOSS P-band SAR in Alaska, ORNL DAAC, <https://doi.org/10.3334/ORNLDAAC/1657>, 2019a.
- 02 Chen, R. H., Bakian-Dogaheh, K., Tabatabaenejad, A., and Moghaddam, M.: Modeling and Retrieving Soil  
03 Moisture and Organic Matter Profiles in the Active Layer of Permafrost Soils From P-Band Radar  
04 Observations, IGARSS 2019 - 2019 IEEE International Geoscience and Remote Sensing Symposium,  
05 10095–10098, <https://doi.org/10.1109/IGARSS.2019.8899802>, 2019b.
- 06 Chen, R. H., Tabatabaenejad, A., and Moghaddam, M.: Retrieval of Permafrost Active Layer Properties Using  
07 Time-Series P-Band Radar Observations, *IEEE Trans. Geosci. Remote Sens.*, *57*, 6037–6054,  
08 <https://doi.org/10.1109/TGRS.2019.2903935>, 2019c.
- 09 Chen, R. H., Michaelides, R. J., Sullivan, T. D., Parsekian, A. D., Zebker, H. A., Moghaddam, M., and Schaefer,  
10 K. M.: Joint Retrieval of Soil Moisture and Permafrost Active Layer Thickness Using L-Band Insar and P-  
11 Band Polsar, IGARSS 2020 - 2020 IEEE International Geoscience and Remote Sensing Symposium, 4606–  
12 4609, <https://doi.org/10.1109/IGARSS39084.2020.9324660>, 2020a.
- 13 Chen, R. H., Pinto, N., Duan, X., Tabatabaenejad, A., and Moghaddam, M.: Mapping Tree Canopy Cover and  
14 Canopy Height with L-Band SAR Using LiDAR Data and Random Forests, IGARSS 2020 - 2020 IEEE  
15 International Geoscience and Remote Sensing Symposium, 4136–4139,  
16 <https://doi.org/10.1109/IGARSS39084.2020.9323738>, 2020b.
- 17 Chen, R. H., Michaelides, R. J., Sullivan, T. D., Parsekian, A. D., Zebker, H. A., Moghaddam, M., & Schaefer,  
18 K. M. (2021a). Joint retrieval of soil moisture and activere layer thickness in the northern circumpolar  
19 permafrost region using l-band InSAR and p-band polsar. *Earth and Space Science*.
- 20 Chen, Richard H., Roger J. Michaelides, Yuhuan Zhao, Lingcao Huang, Elizabeth Wig, Taylor D. Sullivan,  
21 Andrew D. Parsekian, Howard A. Zebker, Mahta Moghaddam, and Kevin M. Schaefer. "Permafrost  
22 Dynamics Observatory: Retrieval of Active Layer Thickness and Soil Moisture from Airborne Insar and  
23 Polsar Data." In *2021 IEEE International Geoscience and Remote Sensing Symposium IGARSS*, pp. 1444-  
24 1447. IEEE, 2021b. DOI: 10.1109/IGARSS47720.2021.9554288
- 25 Colliander, A., Cosh, M. H., Misra, S., Jackson, T. J., Crow, W. T., Powers, J., McNairn, H., Bullock, P., Berg,  
26 A., Magagi, R., Gao, Y., Bindlish, R., Williamson, R., Ramos, I., Latham, B., O'Neill, P., and Yueh, S.:  
27 Comparison of high-resolution airborne soil moisture retrievals to SMAP soil moisture during the SMAP  
28 validation experiment 2016 (SMAPVEX16), *Remote Sens. Environ.*, *227*, 137–150,  
29 <https://doi.org/10.1016/j.rse.2019.04.004>, 2019.
- 30 Cook, B. D., L. W. Corp, R. F. Nelson, E. M. Middleton, D. C. Morton, J. T. McCorkel, J. G. Masek, K. J.  
31 Ranson, V. Ly, and P. M. Montesano (2013): NASA Goddard's Lidar, Hyperspectral and Thermal (G-LiHT)  
32 airborne imager. *Remote Sensing* *5*:4045-4066, doi:10.3390/rs5084045.



- 33 Cooley, S. W., Smith, L. C., Stepan, L., and Mascaro, J.: Tracking Dynamic Northern Surface Water Changes  
34 with High-Frequency Planet CubeSat Imagery, *Remote Sens.*, 9, 1306, <https://doi.org/10.3390/rs9121306>,  
35 2017.
- 36 Crasto, N., Hopkinson, C., Forbes, D. L., Lesack, L., Marsh, P., Spooner, I., and van der Sanden, J. J.: A LiDAR-  
37 based decision-tree classification of open water surfaces in an Arctic delta, *Remote Sens. Environ.*, 164, 90–  
38 102, <https://doi.org/10.1016/j.rse.2015.04.011>, 2015.
- 39 Danby, R.: A Muniscale Study of Tree-Line Dynamics in Southwestern Yukon, Arctic, 56, 427–429, 2003.
- 40 Danby, R. K., Williams, A., and Hik, D. S.: Fifty Years of Science at the Kluane Lake Research Station, Arctic,  
41 67, iii–viii, <https://doi.org/10.14430/arctic4398>, 2014.
- 42 Davey, C. A., Redmond, K. T., and Simeral, D. B.: Weather and Climate Inventory National Park Service  
43 Southwest Alaska Network, National Park Service, Fort Collins, Colorado, 2007.
- 44 Davidson, S. J., Santos, M. J., Sloan, V. L., Watts, J. D., Phoenix, G. K., Oechel, W. C., and Zona, D.: Mapping  
45 Arctic Tundra Vegetation Communities Using Field Spectroscopy and Multispectral Satellite Data in North  
46 Alaska, USA, *Remote Sens.*, 8, 978, <https://doi.org/10.3390/rs8120978>, 2016.
- 47 Davidson, S. J., Santos, M. J., Sloan, V. L., Reuss-Schmidt, K., Phoenix, G. K., Oechel, W. C., and Zona, D.:  
48 Upscaling CH<sub>4</sub> Fluxes Using High-Resolution Imagery in Arctic Tundra Ecosystems, *Remote Sens.*, 9, 1227,  
49 <https://doi.org/10.3390/rs9121227>, 2017.
- 50 Dengel, S. and Torn, M.: NGE Arctic CO<sub>2</sub>, CH<sub>4</sub> and Energy Eddy-Covariance (EC) Flux Tower Auxiliary  
51 Measurements, Council Road Mile Marker 71, Seward Peninsula, Alaska, 2017 - Ongoing,  
52 <https://doi.org/10.5440/1526749>, 2020.
- 53 Douglas, T. A.: ABoVE: Soil Active Layer Thaw Depths at CRREL sites near Fairbanks, Alaska, 2014-2018,  
54 ORNL DAAC, <https://doi.org/10.3334/ORNLDAAC/1701>, 2019.
- 55 Douglas, T. A., Hiemstra, C. A., and Barker, A. J.: ABoVE: End of Season Snow Depth at CRREL sites near  
56 Fairbanks, Alaska, 2014-2019, ORNL DAAC, <https://doi.org/10.3334/ORNLDAAC/1702>, 2019.
- 57 Douglas, T. A., Turetsky, M. R., and Koven, C. D.: Increased rainfall stimulates permafrost thaw across a variety  
58 of Interior Alaskan boreal ecosystems, *Npj Clim. Atmospheric Sci.*, 3, 1–7, <https://doi.org/10.1038/s41612-020-0130-4>, 2020.
- 60 Douglas, T. A., Hiemstra, C. A., Anderson, J. E., Barbato, R. A., Bjella, K. L., Deeb, E. J., Gelvin, A. B., Nelsen,  
61 P. E., Newman, S. D., Saari, S. P., and Wagner, A. M.: Recent degradation of Interior Alaska permafrost  
62 mapped with ground surveys, geophysics, deep drilling, and repeat airborne LiDAR, *Cryosphere Discuss.*, 1–  
63 39, <https://doi.org/10.5194/tc-2021-47>, 2021.
- 64 Du, J., Kimball, J. S., and Moghaddam, M.: Theoretical Modeling and Analysis of L- and P-band Radar  
65 Backscatter Sensitivity to Soil Active Layer Dielectric Variations, *Remote Sens.*, 7, 9450–9472,  
66 <https://doi.org/10.3390/rs70709450>, 2015.
- 67 Engstrom, R., Hope, A., Kwon, H., Stow, D., and Zanolodchikov, D.: Spatial distribution of near surface soil  
68 moisture and its relationship to microtopography in the Alaskan Arctic coastal plain, *Hydrol. Res.*, 36, 219–  
69 234, <https://doi.org/10.2166/nh.2005.0016>, 2005.
- 70 Euskirchen, E. S. and Edgar, C.: FLUXNET-CH<sub>4</sub> US-BZB Bonanza Creek Thermokarst Bog, ,  
71 <https://doi.org/10.18140/FLX/1669668>, 2014a.
- 72 Euskirchen, E. S. and Edgar, C.: FLUXNET-CH<sub>4</sub> US-BZF Bonanza Creek Rich Fen, ,  
73 <https://doi.org/10.18140/FLX/1669669>, 2014b.
- 74 Euskirchen, E. S. and Edgar, C.: FLUXNET-CH<sub>4</sub> US-BZS Bonanza Creek Black Spruce, ,  
75 <https://doi.org/10.18140/FLX/1669670>, 2015.
- 76 Euskirchen, E. S., Bret-Harte, M. S., Scott, G. J., Edgar, C., and Shaver, G. R.: Seasonal patterns of carbon  
77 dioxide and water fluxes in three representative tundra ecosystems in northern Alaska, *Ecosphere*, 3, art4,  
78 <https://doi.org/10.1890/ES11-00202.1>, 2012.



- 79 Fayne, J. V., Smith, L. C., Pitcher, L. H., Kyzivat, E. D., Cooley, S. W., Cooper, M. G., Denbina, M. W., Chen,  
80 A. C., Chen, C. W., and Pavelsky, T. M.: Airborne observations of arctic-boreal water surface elevations  
81 from AirSWOT Ka-Band InSAR and LVIS LiDAR, *Environ. Res. Lett.*, 15, 105005,  
82 <https://doi.org/10.1088/1748-9326/abadcc>, 2020.
- 83 French, N. H. F., Bourgeau-Chavez, L. L., and Chapman, B.: Wetland monitoring in high northern latitudes for  
84 carbon and habitat assessment using synthetic aperture radar, in: AGU Fall Meeting Abstracts, H31N-1951,  
85 2019.
- 86 French, N. H. F., Graham, J. A., Bourgeau-Chavez, L. L., and Whitman, E.: ABoVE: Burn Severity of Soil  
87 Organic Matter, Northwest Territories, Canada, 2014-2015, ORNL DAAC,  
88 <https://doi.org/10.3334/ORNLDAAC/1694>, 2020a.
- 89 French, N. H. F., Graham, J., Whitman, E., Bourgeau-Chavez, L. L., French, N. H. F., Graham, J., Whitman, E.,  
90 and Bourgeau-Chavez, L. L.: Quantifying surface severity of the 2014 and 2015 fires in the Great Slave Lake  
91 area of Canada, *Int. J. Wildland Fire*, 29, 892–906, <https://doi.org/10.1071/WF20008>, 2020b.
- 92 Frost, G. V., Loehman, R. A., Nelson, P. R., and Paradis, D. P.: ABoVE: Vegetation Composition across Fire  
93 History Gradients on the Y-K Delta, Alaska, ORNL DAAC, <https://doi.org/10.3334/ORNLDAAC/1772>,  
94 2020.
- 95 Gamon, J. A., Huemmrich, K. F., Peddle, D. R., Chen, J., Fuentes, D., Hall, F. G., Kimball, J. S., Goetz, S., Gu,  
96 J., McDonald, K. C., Miller, J. R., Moghaddam, M., Rahman, A. F., Roujean, J.-L., Smith, E. A., Walthall, C.  
97 L., Zarco-Tejada, P., Hu, B., Fernandes, R., and Cihlar, J.: Remote sensing in BOREAS: Lessons learned,  
98 *Remote Sens. Environ.*, 89, 139–162, <https://doi.org/10.1016/j.rse.2003.08.017>, 2004.
- 99 Goetz, SJ, Miller, CE, Griffith, PC, et al., An overview of NASA’s Arctic Boreal Vulnerability Experiment  
00 (ABoVE): An integrated research campaign to assess ecosystem vulnerability and its implications within the  
01 Arctic and boreal domain, *Environmental Research Letters* (ABoVE Special Collection), Manuscript ERL-  
02 112259, in revision, 2022
- 03 Greaves, H. E., Vierling, L., Eitel, J., Boelman, N., Magney, T., Prager, C., and Griffin, K.: High-Resolution  
04 Shrub Biomass and Uncertainty Maps, Toolik Lake Area, Alaska, 2013, ORNL DAAC,  
05 <https://doi.org/10.3334/ORNLDAAC/1573>, 2018.
- 06 Gusmeroli, A., Liu, L., Schaefer, K., Zhang, T., Schaefer, T., and Grosse, G.: Active Layer Stratigraphy and  
07 Organic Layer Thickness at a Thermokarst Site in Arctic Alaska Identified Using Ground Penetrating Radar,  
08 *Arct. Antarct. Alp. Res.*, 47, 195–202, <https://doi.org/10.1657/AAAR00C-13-301>, 2015.
- 09 He, J., Loboda, T. V., Jenkins, L., and Chen, D.: Mapping fractional cover of major fuel type components across  
10 Alaskan tundra, *Remote Sens. Environ.*, 232, 111324, <https://doi.org/10.1016/j.rse.2019.111324>, 2019.
- 11 He, J., Loboda, T. V., Jenkins, L., and Chen, D.: ABoVE: Distribution Maps of Wildland Fire Fuel Components  
12 across Alaskan Tundra, 2015, ORNL DAAC, <https://doi.org/10.3334/ORNLDAAC/1761>, 2020.
- 13 He, J., Chen, D., Jenkins, L., and Loboda, T. V.: Impacts of wildfire and landscape factors on organic soil  
14 properties in Arctic tussock tundra. *Environmental Research Letters.*, *Environ. Res. Lett.*, in review, n.d.
- 15 Hensley, S., Oveisgharan, S., Saatchi, S., Simard, M., Ahmed, R. and Haddad, Z., 2014. An error model  
16 for biomass estimates derived from polarimetric radar backscatter. *IEEE Transactions on*  
17 *Geoscience and Remote Sensing*, 52(7), pp.4065-4082.
- 18 Hensley, S., Lou, Y., Michel, T., Muellerschoen, R., Hawkins, B., Laval, M., Pinto, N., Reigber, A.  
19 and Pardini, M., 2016, July. UAVSAR PolInSAR and tomographic experiments in Germany. In  
20 *Geoscience and Remote Sensing Symposium (IGARSS), 2016 IEEE International* (pp. 7517-7520).  
21 IEEE.
- 22 Hensley, S., Chapman, B., Laval, M., Hawkins, B., Riel, B., Michel, T., Muellerschoen, R., Lou, Y., and  
23 Simard, M.: UAVSAR L-Band and P-Band Tomographic Experiments in Boreal Forests, IGARSS 2018 -



- 24 2018 IEEE International Geoscience and Remote Sensing Symposium, 8679–8682,  
25 <https://doi.org/10.1109/IGARSS.2018.8518784>, 2018.
- 26 Hensley, S., Ahmed, R., Chapman, B., Hawkins, B., Lavallo, M., Pinto, N., Pardini, M., Papathanassiou, K.,  
27 Siqueria, P., and Treuhaft, R.: Boreal Forest Radar Tomography at P, L and S-Bands at Berms and Delta  
28 Junction, IGARSS 2020 - 2020 IEEE International Geoscience and Remote Sensing Symposium, 96–99,  
29 <https://doi.org/10.1109/IGARSS39084.2020.9323337>, 2020.
- 30 Higuera, P. E., Barnes, J., Chipman, M. L., Urban, M., and Hu, F. S.: The Burning Tundra: A Look Back at the  
31 Last 6,000 Years of Fire in the Noatak National Preserve, Northwestern Alaska (U.S. National Park Service),  
32 *Alsk. Park Sci.*, 10, 36–41, 2011.
- 33 Hinzman, L. D., Deal, C. J., McGuire, A. D., Mernild, S. H., Polyakov, I. V., and Walsh, J. E.: Trajectory of the  
34 Arctic as an integrated system, *Ecol. Appl.*, 23, 1837–1868, <https://doi.org/10.1890/11-1498.1>, 2013.
- 35 Hogg, E. H., Michaelian, M., Hook, T. I., and Undershultz, M. E.: Recent climatic drying leads to age-  
36 independent growth reductions of white spruce stands in western Canada, *Glob. Change Biol.*, 23, 5297–  
37 5308, <https://doi.org/10.1111/gcb.13795>, 2017.
- 38 Hogg, E. H. (Ted) H. H., Brandt, J. P. B. P., and Michaelian, M. M.: Impacts of a regional drought on the  
39 productivity, dieback, and biomass of western Canadian aspen forests, *Can. J. For. Res.*,  
40 <https://doi.org/10.1139/X08-001>, 2008.
- 41 Holloway, J. E., Lewkowicz, A. G., Douglas, T. A., Li, X., Turetsky, M. R., Baltzer, J. L., and Jin, H.: Impact of  
42 wildfire on permafrost landscapes: A review of recent advances and future prospects, *Permafrost. Periglac.*  
43 *Process.*, 31, 371–382, <https://doi.org/10.1002/ppp.2048>, 2020.
- 44 Hopkinson, C., Crasto, N., Marsh, P., Forbes, D., and Lesack, L.: Investigating the spatial distribution of water  
45 levels in the Mackenzie Delta using airborne LiDAR, *Hydrol. Process.*, 25, 2995–3011,  
46 <https://doi.org/10.1002/hyp.8167>, 2011.
- 47 Horn, R., Jaeger, M., Keller, M., Limbach, M., Nottensteiner, A., Pardini, M., Reigber, A., and Scheiber, R.: F-  
48 SAR - recent upgrades and campaign activities, in: 2017 18th International Radar Symposium (IRS), 2017  
49 18th International Radar Symposium (IRS), 1–10, <https://doi.org/10.23919/IRS.2017.8008092>, 2017.
- 50 Hoy, E. E., Griffith, P., Miller, C. E., and Team, A. S.: ABoVE: Directory of Field Sites Associated with 2017  
51 ABoVE Airborne Campaign, ORNL DAAC, <https://doi.org/10.3334/ORN LDAAC/1582>, 2018.
- 52 Hu, F. S., Higuera, P. E., Walsh, J. E., Chapman, W. L., Duffy, P. A., Brubaker, L. B., and Chipman, M. L.:  
53 Tundra burning in Alaska: Linkages to climatic change and sea ice retreat, *J. Geophys. Res. Biogeosciences*,  
54 115, <https://doi.org/10.1029/2009JG001270>, 2010.
- 55 Iwahana, G., Harada, K., Uchida, M., Tsuyuzaki, S., Saito, K., Narita, K., Kushida, K., and Hinzman, L. D.:  
56 Geomorphological and geochemistry changes in permafrost after the 2002 tundra wildfire in Kougarak,  
57 Seward Peninsula, Alaska, *J. Geophys. Res. Earth Surf.*, 121, 1697–1715,  
58 <https://doi.org/10.1002/2016JF003921>, 2016a.
- 59 Iwahana, G., Uchida, M., Liu, L., Gong, W., Meyer, F. J., Guritz, R., Yamanokuchi, T., and Hinzman, L.: InSAR  
60 Detection and Field Evidence for Thermokarst after a Tundra Wildfire, Using ALOS-PALSAR, *Remote*  
61 *Sens.*, 8, 218, <https://doi.org/10.3390/rs8030218>, 2016b.
- 62 Jafarov, E. E., Parsekian, A. D., Schaefer, K., Liu, L., Chen, A. C., Panda, S. K., and Zhang, T.: Estimating active  
63 layer thickness and volumetric water content from ground penetrating radar measurements in Barrow,  
64 Alaska, *Geosci. Data J.*, 4, 72–79, <https://doi.org/10.1002/gdj3.49>, 2017.
- 65 Jenkins, L. K., Bourgeau-Chavez, L. L., French, N. H. F., Loboda, T. V., and Thelen, B. J.: Development of  
66 Methods for Detection and Monitoring of Fire Disturbance in the Alaskan Tundra Using a Two-Decade Long  
67 Record of Synthetic Aperture Radar Satellite Images, *Remote Sens.*, 6, 6347–6364,  
68 <https://doi.org/10.3390/rs6076347>, 2014.



- 69 Johnston, C. E., Ewing, S. A., Harden, J. W., Varner, R. K., Wickland, K. P., Koch, J. C., Fuller, C. C., Manies,  
70 K., and Jorgenson, M. T.: Effect of permafrost thaw on CO<sub>2</sub> and CH<sub>4</sub> exchange in a western Alaska peatland  
71 chronosequence, *Environ. Res. Lett.*, 9, 085004, <https://doi.org/10.1088/1748-9326/9/8/085004>, 2014.
- 72 Jones, B. M., Kolden, C. A., Jandt, R., Abatzoglou, J. T., Urban, F., and Arp, C. D.: Fire Behavior, Weather, and  
73 Burn Severity of the 2007 Anaktuvuk River Tundra Fire, North Slope, Alaska, *Arct. Antarct. Alp. Res.*, 41,  
74 309–316, <https://doi.org/10.1657/1938-4246-41.3.309>, 2009.
- 75 Jones, B. M., Grosse, G., Arp, C. D., Miller, E., Liu, L., Hayes, D. J., and Larsen, C. F.: Recent Arctic tundra fire  
76 initiates widespread thermokarst development, *Sci. Rep.*, 5, 15865, <https://doi.org/10.1038/srep15865>, 2015.
- 77 Jones, M. C., Harden, J., O'Donnell, J., Manies, K., Jorgenson, T., Treat, C., and Ewing, S.: Rapid carbon loss  
78 and slow recovery following permafrost thaw in boreal peatlands, *Glob. Change Biol.*, 23, 1109–1127,  
79 <https://doi.org/10.1111/gcb.13403>, 2017.
- 80 Jorgenson, M. T., Harden, J., Kanevskiy, M., O'Donnell, J., Wickland, K., Ewing, S., Manies, K., Zhuang, Q.,  
81 Shur, Y., Striegl, R., and Koch, J.: Reorganization of vegetation, hydrology and soil carbon after permafrost  
82 degradation across heterogeneous boreal landscapes, *Environ. Res. Lett.*, 8, 035017,  
83 <https://doi.org/10.1088/1748-9326/8/3/035017>, 2013.
- 84 Karion, A., Sweeney, C., Miller, J. B., Andrews, A. E., Commane, R., Dinardo, S., Henderson, J. M., Lindaas, J.,  
85 Lin, J. C., Luus, K. A., Newberger, T., Tans, P., Wofsy, S. C., Wolter, S., and Miller, C. E.: Investigating  
86 Alaskan methane and carbon dioxide fluxes using measurements from the CARVE tower, *Atmospheric*  
87 *Chem. Phys.*, 16, 5383–5398, <https://doi.org/10.5194/acp-16-5383-2016>, 2016.
- 88 Kobayashi, H., Hiroki, I., and Suzuki, R.: AmeriFlux US-Prr Poker Flat Research Range Black Spruce Forest,  
89 Ver. 3-5, <https://doi.org/10.17190/AMF/1246153>, 2019.
- 90 Kokelj, S. V., Lacelle, D., Lantz, T. C., Tunnicliffe, J., Malone, L., Clark, I. D., and Chin, K. S.: Thawing of  
91 massive ground ice in mega slumps drives increases in stream sediment and solute flux across a range of  
92 watershed scales, *J. Geophys. Res. Earth Surf.*, 118, 681–692, <https://doi.org/10.1002/jgrf.20063>, 2013.
- 93 Kokelj, S. V., Tunnicliffe, J., Lacelle, D., Lantz, T. C., Chin, K. S., and Fraser, R.: Increased precipitation drives  
94 mega slump development and destabilization of ice-rich permafrost terrain, northwestern Canada, *Glob.*  
95 *Planet. Change*, 129, 56–68, <https://doi.org/10.1016/j.gloplacha.2015.02.008>, 2015.
- 96 Kokelj, S. V., Lantz, T. C., Tunnicliffe, J., Segal, R., and Lacelle, D.: Climate-driven thaw of permafrost  
97 preserved glacial landscapes, northwestern Canada, *Geology*, 45, 371–374, <https://doi.org/10.1130/G38626.1>,  
98 2017.
- 99 Kyzivat, E. D., Smith, L. C., Pitcher, L. H., Fayne, J. V., Cooley, S. W., Cooper, M. G., Topp, S. N., Langhorst,  
00 T., Harlan, M. E., Horvat, C., Gleason, C. J., and Pavelsky, T. M.: A High-Resolution Airborne Color-  
01 Infrared Camera Water Mask for the NASA ABoVE Campaign, *Remote Sens.*, 11, 2163,  
02 <https://doi.org/10.3390/rs11182163>, 2019.
- 03 Kyzivat, E. D., Smith, L. C., Pitcher, L. H., Fayne, J. V., Cooley, S. W., Cooper, M. G., Topp, S., Langhorst, T.,  
04 Harlan, M. E., Gleason, C. J., and Pavelsky, T. M.: ABoVE: AirSWOT Water Masks from Color-Infrared  
05 Imagery over Alaska and Canada, 2017, ORNL DAAC, <https://doi.org/10.3334/ORNLDAAC/1707>, 2020.
- 06 Lafleur, P. M. and Humphreys, E. R.: Tundra shrub effects on growing season energy and carbon dioxide  
07 exchange, *Environ. Res. Lett.*, 13, 055001, <https://doi.org/10.1088/1748-9326/aab863>, 2018.
- 08 Lantz, T. C. and Turner, K. W.: Changes in lake area in response to thermokarst processes and climate in Old  
09 Crow Flats, Yukon, *J. Geophys. Res. Biogeosciences*, 120, 513–524, <https://doi.org/10.1002/2014JG002744>,  
10 2015.
- 11 Laval, M., Hawkins, B., and Hensley, S.: Tomographic imaging with UAVSAR: Current status and new results  
12 from the 2016 AfriSAR campaign, 2017 IEEE International Geoscience and Remote Sensing Symposium  
13 (IGARSS), 2485–2488, <https://doi.org/10.1109/IGARSS.2017.8127498>, 2017.



- 14 Le Toan, T., Quegan, S., Davidson, M. W. J., Balzter, H., Paillou, P., Papathanassiou, K., Plummer, S., Rocca, F.,  
15 Saatchi, S., Shugart, H., and Ulander, L.: The BIOMASS mission: Mapping global forest biomass to better  
16 understand the terrestrial carbon cycle, *Remote Sens. Environ.*, 115, 2850–2860,  
17 <https://doi.org/10.1016/j.rse.2011.03.020>, 2011.
- 18 Liljedahl, A., Hinzman, L., Busey, R., and Yoshikawa, K.: Physical short-term changes after a tussock tundra  
19 fire, Seward Peninsula, Alaska, *J. Geophys. Res. Earth Surf.*, 112, <https://doi.org/10.1029/2006JF000554>,  
20 2007.
- 21 Lindsay, C., Zhu, J., Miller, A. E., Kirchner, P., and Wilson, T. L.: Deriving Snow Cover Metrics for Alaska  
22 from MODIS, *Remote Sens.*, 7, 12961–12985, <https://doi.org/10.3390/rs71012961>, 2015.
- 23 Lipovsky, P. S.: Summary of Yukon Geological Survey permafrost monitoring network results, 2008–2013, in:  
24 Yukon Exploration and Geology 2014, edited by: MacFarlane, K. E., Nordling, M. G., and Sack, P. J., Yukon  
25 Geological Survey, 113–122, 2015.
- 26 Liu, L., Schaefer, K., Zhang, T., and Wahr, J.: Estimating 1992–2000 average active layer thickness on the  
27 Alaskan North Slope from remotely sensed surface subsidence, *J. Geophys. Res. Earth Surf.*, 117,  
28 <https://doi.org/10.1029/2011JF002041>, 2012.
- 29 Liu, L., Jafarov, E. E., Schaefer, K. M., Jones, B. M., Zebker, H. A., Williams, C. A., Rogan, J., and Zhang, T.:  
30 InSAR detects increase in surface subsidence caused by an Arctic tundra fire, *Geophys. Res. Lett.*, 41, 3906–  
31 3913, <https://doi.org/10.1002/2014GL060533>, 2014.
- 32 Liu, L., Schaefer, K., Chen, A. C., Gusmeroli, A., Jafarov, E. E., Panda, S. K., Parsekian, A. D., Schaefer, T.,  
33 Zebker, H. A., and Zhang, T.: Pre-ABoVE: Remotely Sensed Active Layer Thickness, Barrow, Alaska, 2006–  
34 2011, ORNL DAAC, <https://doi.org/10.3334/ORNLDAAAC/1266>, 2015a.
- 35 Liu, L., Schaefer, K., Chen, A. C., Gusmeroli, A., Jafarov, E. E., Panda, S. K., Parsekian, A. D., Schaefer, T.,  
36 Zebker, H. A., and Zhang, T.: Pre-ABoVE: Remotely Sensed Active Layer Thickness, Prudhoe Bay, Alaska,  
37 1992–2000, ORNL DAAC, <https://doi.org/10.3334/ORNLDAAAC/1267>, 2015b.
- 38 Loboda, T. V., French, N. H. F., Hight-Harf, C., Jenkins, L., and Miller, M. E.: Mapping fire extent and burn  
39 severity in Alaskan tussock tundra: An analysis of the spectral response of tundra vegetation to wildland fire,  
40 *Remote Sens. Environ.*, 134, 194–209, <https://doi.org/10.1016/j.rse.2013.03.003>, 2013.
- 41 Loboda, T.V., L.K. Jenkins, D. Chen, J. He, and A. Baer. 2022. Burned and Unburned Field Site Data, Noatak,  
42 Seward, and North Slope, AK, 2016–2018. ORNL DAAC, Oak Ridge, Tennessee,  
43 USA. <https://doi.org/10.3334/ORNLDAAAC/1919>
- 44 Lopez-Sanchez, J. M., Ballester-Berman, J. D., Vicente-Guijalba, F., Cloude, S. R., McNairn, H., Shang, J.,  
45 Skriver, H., Jagdhuber, T., Hajnsek, I., Pottier, E., Marechal, C., Hubert-Moy, L., Corgne, S., Wdowinski, S.,  
46 Touzi, R., Gosselin, G., Brooks, R., Yamaguchi, Y., and Singh, G.: Agriculture and Wetland Applications,  
47 in: *Polarimetric Synthetic Aperture Radar: Principles and Application*, vol. 25, edited by: Hajnsek, I. and  
48 Desnos, Y.-L., Springer International Publishing, Cham, 119–178, [https://doi.org/10.1007/978-3-030-56504-](https://doi.org/10.1007/978-3-030-56504-6_3)  
49 [6\\_3](https://doi.org/10.1007/978-3-030-56504-6_3), 2021.
- 50 Lou, Y., Shimada, J. G., Michel, T. R., Muellerschoen, R. J., Zheng, Y., and Moghaddam, M.: Pre-ABoVE: L1  
51 S-0 Polarimetric Data from AirMOSS P-band SAR, Alaska, 2014–2015, ORNL DAAC,  
52 <https://doi.org/10.3334/ORNLDAAAC/1678>, 2019.
- 53 Mack, M. C., Bret-Harte, M. S., Hollingsworth, T. N., Jandt, R. R., Schuur, E. A. G., Shaver, G. R., and Verbyla,  
54 D. L.: Carbon loss from an unprecedented Arctic tundra wildfire, *Nature*, 475, 489–492,  
55 <https://doi.org/10.1038/nature10283>, 2011.
- 56 Magagi, R., Berg, A. A., Goita, K., Belair, S., Jackson, T. J., Toth, B., Walker, A., McNairn, H., O’Neill, P. E.,  
57 Moghaddam, M., Gherboudj, I., Colliander, A., Cosh, M. H., Burgin, M., Fisher, J. B., Kim, S.-B.,  
58 Mladenova, I., Djamai, N., Rousseau, L.-P. B., Belanger, J., Shang, J., and Merzouki, A.: Canadian



- 59 Experiment for Soil Moisture in 2010 (CanEx-SM10): Overview and Preliminary Results, *IEEE Trans.*  
60 *Geosci. Remote Sens.*, 51, 347–363, <https://doi.org/10.1109/TGRS.2012.2198920>, 2013.
- 61 Malone, T., Liang, J., and Packee, E. C.: Cooperative Alaska Forest Inventory, Gen Tech Rep PNW-GTR-785  
62 Portland US Dep. Agric. For. Serv. Pac. Northwest Res. Stn. 42 P, 785, [https://doi.org/10.2737/PNW-GTR-](https://doi.org/10.2737/PNW-GTR-785)  
63 785, 2009.
- 64 Marsh, P., Russell, M., Pohl, S., Haywood, H., and Onclin, C.: Changes in thaw lake drainage in the Western  
65 Canadian Arctic from 1950 to 2000, *Hydrol. Process.*, 23, 145–158, <https://doi.org/10.1002/hyp.7179>, 2009a.
- 66 Marsh, P., Lesack, L., Hicks, F., Roberts, A., Hopkinson, C., Solomon, S., Forbes, D., Russell, M., and Haywood,  
67 H.: Hydrology of the Mackenzie Delta: off-channel water storage and delta interaction with the Beaufort Sea,  
68 2009b.
- 69 Marsh, P., Bartlett, P., MacKay, M., Pohl, S., and Lantz, T.: Snowmelt energetics at a shrub tundra site in the  
70 western Canadian Arctic, *Hydrol. Process.*, 24, 3603–3620, <https://doi.org/10.1002/hyp.7786>, 2010.
- 71 McCune, B., Arup, U., Breuss, O., Di Meglio, J., Esslinger, T. L., Magain, N., Miadlikowska, J., Miller, A. E.,  
72 Muggia, L., Nelson, P. R., Rosentreter, R., Schultz, M., Sheard, J. W., Tønsberg, T., and Walton, J.:  
73 Biodiversity and ecology of lichens of Katmai and Lake Clark National Parks and Preserves, Alaska,  
74 *Mycosphere*, 9, 859–930, 2018.
- 75 McGuire, A. D., Anderson, L. G., Christensen, T. R., Dallimore, S., Guo, L., Hayes, D. J., Heimann, M.,  
76 Lorenson, T. D., Macdonald, R. W., and Roulet, N.: Sensitivity of the carbon cycle in the Arctic to climate  
77 change, *Ecol. Monogr.*, 79, 523–555, <https://doi.org/10.1890/08-2025.1>, 2009.
- 78 Meddens, A. J. H., Vierling, L. A., Eitel, J. U. H., Jennewein, J. S., White, J. C., and Wulder, M. A.: Developing  
79 5 m resolution canopy height and digital terrain models from WorldView and ArcticDEM data, *Remote Sens.*  
80 *Environ.*, 218, 174–188, <https://doi.org/10.1016/j.rse.2018.09.010>, 2018.
- 81 Mehra, R. and Ramanujam, V. M.: L S Band Airborne SAR Data Products Calibration, in: 2019 URSI Asia-  
82 Pacific Radio Science Conference (AP-RASC), 2019 URSI Asia-Pacific Radio Science Conference (AP-  
83 RASC), 1–1, <https://doi.org/10.23919/URSIAP-RASC.2019.8738681>, 2019.
- 84 Meyer, G., Humphreys, E. R., Melton, J. R., Cannon, A. J., and Lafleur, P. M.: Simulating shrubs and their  
85 energy and carbon dioxide fluxes in Canada’s Low Arctic with the Canadian Land Surface Scheme Including  
86 biogeochemical Cycles (CLASSIC), *Biogeosciences Discuss.*, 1–34, <https://doi.org/10.5194/bg-2020-458>,  
87 2020.
- 88 Michaelian, M., Hogg, E. H., Hall, R. J., and Arseneault, E.: Massive mortality of aspen following severe drought  
89 along the southern edge of the Canadian boreal forest, *Glob. Change Biol.*, 17, 2084–2094,  
90 <https://doi.org/10.1111/j.1365-2486.2010.02357.x>, 2011.
- 91 Michaelides, R. J., Schaefer, K., Zebker, H. A., Parsekian, A., Liu, L., Chen, J., Natali, S., Ludwig, S., and  
92 Schaefer, S. R.: Inference of the impact of wildfire on permafrost and active layer thickness in a  
93 discontinuous permafrost region using the remotely sensed active layer thickness (ReSALT) algorithm,  
94 *Environ. Res. Lett.*, 14, 035007, <https://doi.org/10.1088/1748-9326/aaf932>, 2019.
- 95 Michaelides, R. J., Chen, R. H., Zhao, Y., Schaefer, K., Parsekian, A. D., Sullivan, T., et al. (2021).  
96 Permafrost Dynamics Observatory—part I: Postprocessing and calibration methods of UAVSAR L-  
97 band InSAR data for seasonal subsidence estimation. *Earth and Space Science*, 8, e2020EA001630.  
98 <https://doi.org/10.1029/2020EA001630>
- 99 Miller, C. E., Griffith, P. C., Goetz, S. J., Hoy, E. E., Pinto, N., McCubbin, I. B., Thorpe, A. K., Hofton, M.,  
00 Hodkinson, D., Hansen, C., Woods, J., Larson, E., Kasischke, E. S., and Margolis, H. A.: An overview of  
01 ABoVE airborne campaign data acquisitions and science opportunities, *Environ. Res. Lett.*, 14, 080201,  
02 <https://doi.org/10.1088/1748-9326/ab0d44>, 2019.



- 03 Miller, C.E., P. Griffith, E.E. Hoy, N. Pinto, Y. Lou, S. Hensley, B. Chapman, J.L. Baltzer, K. Bakian-  
04 Dogaheh, W.R. Bolton, L.L. Bourgeau-Chavez, R.H. Chen, B-H. Choe, L.K. Clayton, T.A.  
05 Douglas, N.H.F. French, J.E. Holloway, G. Hong, L. Huang, G. Iwahana, L.K. Jenkins, J.S.  
06 Kimball, T.V. Loboda, M.C. Mack, P. Marsh, R.J. Michaelides, M. Moghaddam, A.D. Parsekian, K.  
07 Schaefer, P. Siqueira, D. Singh, A. Tabatabaenejad, M.R. Turetsky, R. Touzi, E. Wig, P. Wilson,  
08 C.J. Wilson, S.D. Wullschleger, Y. Yi, H.A. Zebker, Y. Zhang, Y. Zhao, and S.J. Goetz. 2023.  
09 Summary of the ABoVE L-band and P-band Airborne SAR Surveys. ORNL DAAC, Oak Ridge,  
10 Tennessee, USA. <https://doi.org/10.3334/ORNLDAAC/2150>
- 11 Minions, C., Natali, S., Watts, J. D., Ludwig, S., and Risk, D.: ABoVE: Year-Round Soil CO<sub>2</sub> Efflux in Alaskan  
12 Ecosystems, Version 2, ORNL DAAC, <https://doi.org/10.3334/ORNLDAAC/1762>, 2020.
- 13 Minsley, B. J., Abraham, J. D., Smith, B. D., Cannia, J. C., Voss, C. I., Jorgenson, M. T., Walvoord, M. A.,  
14 Wylie, B. K., Anderson, L., Ball, L. B., Deszcz-Pan, M., Wellman, T. P., and Ager, T. A.: Airborne  
15 electromagnetic imaging of discontinuous permafrost, *Geophys. Res. Lett.*, 39,  
16 <https://doi.org/10.1029/2011GL050079>, 2012.
- 17 Moghaddam, M., Tabatabaenejad, A., Chen, R. H., Saatchi, S. S., Jaruwatanadilok, S., Burgin, M., Duan, X.,  
18 and Truong-Loi, M. L.: AirMOSS: L2/3 Volumetric Soil Moisture Profiles Derived From Radar, 2012-2015,  
19 ORNL DAAC, <https://doi.org/10.3334/ORNLDAAC/1418>, 2016.
- 20 Montesano, P. M., Sun, G., Dubayah, R. O., and Ranson, K. J.: Spaceborne potential for examining taiga–tundra  
21 ecotone form and vulnerability, *Biogeosciences*, 13, 3847–3861, <https://doi.org/10.5194/bg-13-3847-2016>,  
22 2016.
- 23 Myers-Smith, I. H., Forbes, B. C., Wilmking, M., Hallinger, M., Lantz, T., Blok, D., Tape, K. D., Macias-Fauria,  
24 M., Sass-Klaassen, U., Lévesque, E., Boudreau, S., Ropars, P., Hermanutz, L., Trant, A., Collier, L. S.,  
25 Weijers, S., Rozema, J., Rayback, S. A., Schmidt, N. M., Schaepman-Strub, G., Wipf, S., Rixen, C., Ménard,  
26 C. B., Venn, S., Goetz, S., Andreu-Hayles, L., Elmendorf, S., Ravolainen, V., Welker, J., Grogan, P., Epstein,  
27 H. E., and Hik, D. S.: Shrub expansion in tundra ecosystems: dynamics, impacts and research priorities,  
28 *Environ. Res. Lett.*, 6, 045509, <https://doi.org/10.1088/1748-9326/6/4/045509>, 2011.
- 29 Natali, S. M., Schuur, E. A. G., Webb, E. E., Pries, C. E. H., and Crummer, K. G.: Permafrost degradation  
30 stimulates carbon loss from experimentally warmed tundra, *Ecology*, 95, 602–608,  
31 <https://doi.org/10.1890/13-0602.1>, 2014.
- 32 National Research Council: Opportunities to Use Remote Sensing in Understanding Permafrost and Related  
33 Ecological Characteristics: Report of a Workshop, The National Academies Press, Washington, DC, 2014.
- 34 Oechel, W. C., Vourlitis, G. L., Hastings, S. J., Zulueta, R. C., Hinzman, L., and Kane, D.: Acclimation of  
35 ecosystem CO<sub>2</sub> exchange in the Alaskan Arctic in response to decadal climate warming, *Nature*, 406, 978–  
36 981, <https://doi.org/10.1038/35023137>, 2000.
- 37 Pan, C. G., Kirchner, P. B., Kimball, J. S., and Du, J.: A Long-Term Passive Microwave Snowoff Record for the  
38 Alaska Region 1988–2016, *Remote Sens.*, 12, 153, <https://doi.org/10.3390/rs12010153>, 2020.
- 39 Pavelsky, T. M. and Smith, L. C.: Remote sensing of hydrologic recharge in the Peace-Athabasca Delta, Canada,  
40 *Geophys. Res. Lett.*, 35, <https://doi.org/10.1029/2008GL033268>, 2008.
- 41 Pietroniro, A., Peters, D. L., Yang, D., Fiset, J.-M., Saint-Jean, R., Fortin, V., Leconte, R., Bergeron, J., Siles, G.  
42 L., Trudel, M., Garnaud, C., Matte, P., Smith, L. C., Gleason, C. J., and Pavelsky, T. M.: Canada's  
43 Contributions to the SWOT Mission – Terrestrial Hydrology (SWOT-C TH), *Can. J. Remote Sens.*, 45, 116–  
44 138, <https://doi.org/10.1080/07038992.2019.1581056>, 2019.
- 45 Pitcher, L. H., Smith, L. C., Pavelsky, T. M., Fayne, J. V., Cooley, S. W., Altenau, E. H., Moller, D. K., and  
46 Arvesen, J.: ABoVE: AirSWOT Radar, Orthomosaic, and Water Masks, Yukon Flats Basin, Alaska, 2015,  
47 ORNL DAAC, <https://doi.org/10.3334/ORNLDAAC/1655>, 2019a.





- 48 Pitcher, L. H., Pavelsky, T. M., Smith, L. C., Moller, D. K., Altenau, E. H., Allen, G. H., Lion, C., Butman, D.,  
49 Cooley, S. W., Fayne, J. V., and Bertram, M.: AirSWOT InSAR Mapping of Surface Water Elevations and  
50 Hydraulic Gradients Across the Yukon Flats Basin, Alaska, *Water Resour. Res.*, 55, 937–953,  
51 <https://doi.org/10.1029/2018WR023274>, 2019b.
- 52 Pitcher, L. H., Smith, L. C., Cooley, S. W., Zaino, A., Carlson, R., Pettit, J., Gleason, C. J., Minear, J. T., Fayne,  
53 J. V., Willis, M. J., Hansen, J. S., Easterday, K. J., Harlan, M. E., Langhorst, T., Topp, S. N., Dolan, W.,  
54 Kyzivat, E. D., Pietroniro, A., Marsh, P., Yang, D., Carter, T., Onclin, C., Hosseini, N., Wilcox, E., Moreira,  
55 D., Berge-Nguyen, M., Cretaux, J.-F., and Pavelsky, T. M.: Advancing Field-Based GNSS Surveying for  
56 Validation of Remotely Sensed Water Surface Elevation Products, *Front. Earth Sci.*, 8,  
57 <https://doi.org/10.3389/feart.2020.00278>, 2020.
- 58 Plaza, C., Pegoraro, E., Bracho, R., Celis, G., Crummer, K. G., Hutchings, J. A., Hicks Pries, C. E., Mauritz, M.,  
59 Natali, S. M., Salmon, V. G., Schädel, C., Webb, E. E., and Schuur, E. A. G.: Direct observation of  
60 permafrost degradation and rapid soil carbon loss in tundra, *Nat. Geosci.*, 12, 627–631,  
61 <https://doi.org/10.1038/s41561-019-0387-6>, 2019.
- 62 Porter, C., Morin, P., Howat, I., Noh, M.-J., Bates, B., Peterman, K., Keeseey, S., Schlenk, M., Gardiner, J.,  
63 Tomko, K., Willis, M., Kelleher, C., Cloutier, M., Husby, E., Foga, S., Nakamura, H., Platson, M.,  
64 Wethington, M., Williamson, C., Bauer, G., Enos, J., Arnold, G., Kramer, W., Becker, P., Doshi, A.,  
65 D’Souza, C., Cummens, P., Laurier, F., and Bojesen, M.: ArcticDEM,  
66 <https://doi.org/10.7910/DVN/OHHUKH>, 2018.
- 67 Potter, C.: Ecosystem carbon emissions from 2015 forest fires in interior Alaska, *Carbon Balance Manag.*, 13, 2,  
68 <https://doi.org/10.1186/s13021-017-0090-0>, 2018.
- 69 Quegan, S., Le Toan, T., Chave, J., Dall, J., Exbrayat, J.-F., Minh, D. H. T., Lomas, M., D’Alessandro, M. M.,  
70 Paillou, P., Papathanassiou, K., Rocca, F., Saatchi, S., Scipal, K., Shugart, H., Smallman, T. L., Soja, M. J.,  
71 Tebaldini, S., Ulander, L., Villard, L., and Williams, M.: The European Space Agency BIOMASS mission:  
72 Measuring forest above-ground biomass from space, *Remote Sens. Environ.*, 227, 44–60,  
73 <https://doi.org/10.1016/j.rse.2019.03.032>, 2019.
- 74 Quinton, W., Berg, A., Braverman, M., Carpino, O., Chasmer, L., Connon, R., Craig, J., Devoie, É., Hayashi, M.,  
75 Haynes, K., Olefeldt, D., Pietroniro, A., Rezanezhad, F., Schincariol, R., and Sonntag, O.: A synthesis of  
76 three decades of hydrological research at Scotty Creek, NWT, Canada, *Hydrol. Earth Syst. Sci.*, 23, 2015–  
77 2039, <https://doi.org/10.5194/hess-23-2015-2019>, 2019.
- 78 Quinton, W. L., Adams, J. R., Baltzer, J. L., Berg, A. A., Craig, J. R., and Johnson, E.: Permafrost Ecosystems in  
79 Transition: Understanding and Predicting Hydrological and Ecological Change in the Southern Taiga Plains,  
80 Northeastern British Columbia and Southwestern Northwest Territories, 6, 2015.
- 81 Ramanujam, V. M. and Mehra, R.: L S Band SAR Data Processing and Products, in: 2019 URSI Asia-Pacific  
82 Radio Science Conference (AP-RASC), 2019 URSI Asia-Pacific Radio Science Conference (AP-RASC), 1–  
83 1, <https://doi.org/10.23919/URSIAP-RASC.2019.8738235>, 2019.
- 84 Ramanujam, V. M., Suneela, T. J. V. D., and Bhan, R.: ISRO’s dual frequency airborne SAR pre-cursor to  
85 NISAR, in: Earth Observing Missions and Sensors: Development, Implementation, and Characterization IV,  
86 Earth Observing Missions and Sensors: Development, Implementation, and Characterization IV, 98810A,  
87 <https://doi.org/10.1117/12.2228086>, 2016.
- 88 Rocha, A. V. and Shaver, G. R.: Burn severity influences postfire CO<sub>2</sub> exchange in arctic tundra, *Ecol. Appl.*, 21,  
89 477–489, <https://doi.org/10.1890/10-0255.1>, 2011a.
- 90 Rocha, A. V. and Shaver, G. R.: Postfire energy exchange in arctic tundra: the importance and climatic  
91 implications of burn severity, *Glob. Change Biol.*, 17, 2831–2841, <https://doi.org/10.1111/j.1365-2486.2011.02441.x>, 2011b.



- 93 Rosen, P.A., Kim, Y., Kumar, R., Misra, T., Bhan, R. and Sagi, V.R., 2017, May. Global persistent SAR  
94 sampling with the NASA-ISRO SAR (NISAR) mission. In *Radar Conference (RadarConf), 2017 IEEE* (pp.  
95 0410-0414). IEEE.
- 96 Roy, A., Toose, P., Mavrovic, A., Pappas, C., Royer, A., Derksen, C., Berg, A., Rowlandson, T., El-Amine, M.,  
97 Barr, A., Black, A., Langlois, A., and Sonnentag, O.: L-Band response to freeze/thaw in a boreal forest stand  
98 from ground- and tower-based radiometer observations, *Remote Sens. Environ.*, 237, 111542,  
99 <https://doi.org/10.1016/j.rse.2019.111542>, 2020.
- 00 Saatchi, S. S. and Moghaddam, M.: Estimation of crown and stem water content and biomass of boreal forest  
01 using polarimetric SAR imagery, *IEEE Trans. Geosci. Remote Sens.*, 38, 697–709,  
02 <https://doi.org/10.1109/36.841999>, 2000.
- 03 Saatchi, S., Xu, L., Yang, Y., and Yu, Y.: Evaluation of NISAR Biomass Algorithm in Temperate and Boreal  
04 Forests, *IGARSS 2019 - 2019 IEEE International Geoscience and Remote Sensing Symposium*, 7363–7366,  
05 <https://doi.org/10.1109/IGARSS.2019.8898657>, 2019.
- 06 Sadeghi, M., Tabatabaenejad, A., Tuller, M., Moghaddam, M., and Jones, S. B.: Advancing NASA’s AirMOSS  
07 P-Band Radar Root Zone Soil Moisture Retrieval Algorithm via Incorporation of Richards’ Equation,  
08 *Remote Sens.*, 9, 17, <https://doi.org/10.3390/rs9010017>, 2017.
- 09 Schaefer, K., Chen, A. C., Chen, J., Chen, R. H., Dogaheh, K., Jafarov, E., Liu, L., Michaelides, R. J.,  
10 Moghaddam, M., Parsekian, A. D., Sullivan, T. D., Tabatabaenejad, A., Thompson, J., and Zebker, H.: The  
11 Permafrost Dynamics Observatory, 2018a.
- 12 Schaefer, K., Chen, A. C., Chen, J., Chen, R. H., Dogaheh, K., Jafarov, E., Liu, L., Michaelides, R. J.,  
13 Moghaddam, M., Parsekian, A. D., Sullivan, T. D., Tabatabaenejad, A., Thompson, J., and Zebker, H.: The  
14 Permafrost Dynamics Observatory (PDO), 2018b.
- 15 Schaefer, K., Michaelides, R. J., Chen, R. H., Sullivan, T. D., Parsekian, A. D., Bakian-Dogaheh, K.,  
16 Tabatabaenejad, A., Moghaddam, M., Chen, J., Chen, A. C., Liu, L., and Zebker, H. A.: ABoVE: Active  
17 Layer Thickness Derived from Airborne L- and P-band SAR, Alaska, 2017, ORNL DAAC,  
18 <https://doi.org/10.3334/ORNLDAAAC/1676>, 2019.
- 19 Schaefer, K., R.J. Michaelides, R.H. Chen, T.D. Sullivan, A.D. Parsekian, Y. Zhao, K. Bakian-Dogaheh, A.  
20 Tabatabaenejad, M. Moghaddam, J. Chen, A.C. Chen, L. Liu, and H.A. Zebker. 2021a. ABoVE: Active  
21 Layer Thickness Derived from Airborne L- and P-band SAR, Alaska, 2017. ORNL DAAC, Oak Ridge,  
22 Tennessee, USA. <https://doi.org/10.3334/ORNLDAAAC/1796>
- 23 Schaefer, K., L.K. Clayton, M.J. Battaglia, L.L. Bourgeau-Chavez, R.H. Chen, A.C. Chen, J. Chen, K. Bakian-  
24 Dogaheh, T.A. Douglas, S.E. Grelick, G. Iwahana, E. Jafarov, L. Liu, S. Ludwig, R.J. Michaelides, M.  
25 Moghaddam, S. Natali, S.K. Panda, A.D. Parsekian, A.V. Rocha, S.R. Schaefer, T.D. Sullivan, A.  
26 Tabatabaenejad, K. Wang, C.J. Wilson, H.A. Zebker, T. Zhang, and Y. Zhao. 2021b. ABoVE: Soil Moisture  
27 and Active Layer Thickness in Alaska and NWT, Canada, 2008-2020. ORNL DAAC, Oak Ridge, Tennessee,  
28 USA. <https://doi.org/10.3334/ORNLDAAAC/1903>
- 29 Schuur, E. A. G., Vogel, J. G., Crummer, K. G., Lee, H., Sickman, J. O., and Osterkamp, T. E.: The effect of  
30 permafrost thaw on old carbon release and net carbon exchange from tundra, *Nature*, 459, 556–559,  
31 <https://doi.org/10.1038/nature08031>, 2009.
- 32 Schuur, T.: AmeriFlux US-EML Eight Mile Lake Permafrost thaw gradient, Healy Alaska (3.5),  
33 <https://doi.org/10.17190/AMF/1418678>, 2019.
- 34 Sellers, P., Hall, F., Margolis, H., Kelly, B., Baldocchi, D., Hartog, G. den, Cihlar, J., Ryan, M. G., Goodison, B.,  
35 Crill, P., Ranson, K. J., Lettenmaier, D., and Wickland, D. E.: The Boreal Ecosystem–Atmosphere Study  
36 (BOREAS): An Overview and Early Results from the 1994 Field Year, *Bull. Am. Meteorol. Soc.*, 76, 1549–  
37 1577, [https://doi.org/10.1175/1520-0477\(1995\)076<1549:TBESAO>2.0.CO;2](https://doi.org/10.1175/1520-0477(1995)076<1549:TBESAO>2.0.CO;2), 1995.



- 38 Sellers, P. J., Hall, F. G., Kelly, R. D., Black, A., Baldocchi, D., Berry, J., Ryan, M., Ranson, K. J., Crill, P. M.,  
39 Lettenmaier, D. P., Margolis, H., Cihlar, J., Newcomer, J., Fitzjarrald, D., Jarvis, P. G., Gower, S. T.,  
40 Halliwell, D., Williams, D., Goodison, B., Wickland, D. E., and Guertin, F. E.: BOREAS in 1997:  
41 Experiment overview, scientific results, and future directions, *J. Geophys. Res. Atmospheres*, 102, 28731–  
42 28769, <https://doi.org/10.1029/97JD03300>, 1997.
- 43 Serrouya, R., Dickie, M., Lamb, C., van Oort, H., Kelly, A. P., DeMars, C., McLoughlin, P. D., Larter, N. C.,  
44 Hervieux, D., Ford, A. T., and Boutin, S.: Trophic consequences of terrestrial eutrophication for a threatened  
45 ungulate, *Proc. R. Soc. B Biol. Sci.*, 288, 20202811, <https://doi.org/10.1098/rspb.2020.2811>, 2021.
- 46 Sherriff, R. L., Miller, A. E., Muth, K., Schriver, M., and Batzel, R.: Spruce growth responses to warming vary  
47 by ecoregion and ecosystem type near the forest-tundra boundary in south-west Alaska, *J. Biogeogr.*, 44,  
48 1457–1468, <https://doi.org/10.1111/jbi.12968>, 2017.
- 49 Shugar, D. H., Clague, J. J., Best, J. L., Schoof, C., Willis, M. J., Copland, L., and Roe, G. H.: River piracy and  
50 drainage basin reorganization led by climate-driven glacier retreat, *Nat. Geosci.*, 10, 370–375,  
51 <https://doi.org/10.1038/ngeo2932>, 2017.
- 52 Silva, C. A., Duncanson, L., Hancock, S., Neuenschwander, A., Thomas, N., Hofton, M., Fatoyinbo, L., Simard,  
53 M., Marshak, C. Z., Armston, J., Lutchke, S., and Dubayah, R.: Fusing simulated GEDI, ICESat-2 and  
54 NISAR data for regional aboveground biomass mapping, *Remote Sens. Environ.*, 253, 112234,  
55 <https://doi.org/10.1016/j.rse.2020.112234>, 2021.
- 56 Smith, L. C., Pavelsky, T., Lettenmaier, D. P., Gleason, C. J., Pietroniro, A., Applejohn, A., Arvesen, J. C.,  
57 Bjella, K., Carter, T., Chao, R., Cooley, S. W., Cooper, M. G., Cretaux, J. F., Douglass, T., Faria, D., Fayne,  
58 J., Fiset, J. M., Goodman, S., Hanna, B., Harlan, M., Langhorst, T., Marsh, P., Moreira, D. M., Minear, J. T.,  
59 Onclin, C., Overstreet, B. T., Peters, D., Pettit, J., Pitcher, L. H., Russell, M., Spence, C., Topp, S., Turner, K.  
60 W., Vimal, S., Wilcox, E., Woodward, J., Yang, D., and Zaino, A.: AirSWOT flights and field campaigns for  
61 the 2017 Arctic-Boreal Vulnerability Experiment (ABOVE), in: AGU Fall Meeting Abstracts, C21F-1176,  
62 2017a.
- 63 Smith, S. L., Roy, L.-P., Lewkowicz, A. G., and Chartrand, J.: Ground thermal data collection along the Alaska  
64 Highway corridor (KP1559-1895), Yukon, summer 2016, Geological Survey of Canada, 2017b.
- 65 Spence, C. and Hedstrom, N.: Hydrometeorological data from Baker Creek Research Watershed, Northwest  
66 Territories, Canada, *Earth Syst. Sci. Data*, 10, 1753–1767, <https://doi.org/10.5194/essd-10-1753-2018>, 2018.
- 67 Sun, G., K. J. Ranson, D. S. Kimes, J. B. Blair, and K. Kovacs (2008), Forest vertical structure from GLAS: An  
68 evaluation using LVIS and SRTM data, *Remote Sens. Environ.*, **112**, 107–117, doi:10.1016/j.rse.2006.09.036.
- 69 Tabatabaenejad, A., and M. Moghaddam, 2011. Retrieval of surface and deep soil moisture and effect  
70 of moisture profile on inversion accuracy. *IEEE Geosci. Remote Sensing Lett.*, vol. 8, no. 3, pp.  
71 477- 481, May 2011.
- 72 Tabatabaenejad, A., Burgin, M., Duan, X., and Moghaddam, M.: P-Band Radar Retrieval of Subsurface Soil  
73 Moisture Profile as a Second-Order Polynomial: First AirMOSS Results, *IEEE Trans. Geosci. Remote Sens.*,  
74 53, 645–658, <https://doi.org/10.1109/TGRS.2014.2326839>, 2015.
- 75 Tabatabaenejad, A., Chen, R. H., Burgin, M. S., Duan, X., Cuenca, R. H., Cosh, M. H., Scott, R. L., and  
76 Moghaddam, M.: Assessment and Validation of AirMOSS P-Band Root-Zone Soil Moisture Products, *IEEE*  
77 *Trans. Geosci. Remote Sens.*, 58, 6181–6196, <https://doi.org/10.1109/TGRS.2020.2974976>, 2020.
- 78 Tank, S., Olefeldt, D., Department of Renewable Resources, University of Alberta, Edmonton, Alberta, Canada,  
79 Quinton, W., Centre for Cold Regions and Water Science, Wilfred Laurier University, Waterloo, Ontario,  
80 Canada, Spence, C., Environment and Climate Change Canada, Saskatoon, Saskatchewan, Canada, Dion, N.,  
81 Water Resources Department, Government of Northwest Territories, Yellowknife, Northwest Territories,  
82 Canada, Ackley, C., Centre for Cold Regions and Water Science, Wilfred Laurier University, Waterloo,  
83 Ontario, Canada, Burd, K., Department of Renewable Resources, University of Alberta, Edmonton, Alberta,



- 84 Canada, Hutchins, R., Department of Biological Sciences, University of Alberta, Edmonton, Alberta, Canada,  
85 Mengistu, S., and Department of Biological Sciences, University of Alberta, Edmonton, Alberta, Canada:  
86 Fire in the Arctic: The effect of wildfire across diverse aquatic ecosystems of the Northwest Territories, *Polar*  
87 *Knowl. Aqhaliat Rep.*, 1, 31–38, <https://doi.org/10.35298/pkc.2018.04>, 2019.
- 88 Touzi, R., Deschamps, A., and Rother, G.: Phase of Target Scattering for Wetland Characterization Using  
89 Polarimetric C-Band SAR, *IEEE Trans. Geosci. Remote Sens.*, 47, 3241–3261,  
90 <https://doi.org/10.1109/TGRS.2009.2018626>, 2009.
- 91 Touzi, R., Omari, K., Sleep, B., and Jiao, X.: Scattered and Received Wave Polarization Optimization for  
92 Enhanced Peatland Classification and Fire Damage Assessment Using Polarimetric PALSAR, *IEEE J. Sel.*  
93 *Top. Appl. Earth Obs. Remote Sens.*, PP, 1–26, <https://doi.org/10.1109/JSTARS.2018.2873740>, 2018.
- 94 Touzi, R., Hong, G., Motohka, T., Shinichi, S., and De Lisle, D.: Investigation of Compact SAR L and C band  
95 Complementarity for Permafrost Characterization In Arctic Regions, *IGARSS 2019 - 2019 IEEE*  
96 *International Geoscience and Remote Sensing Symposium*, 4665–4667,  
97 <https://doi.org/10.1109/IGARSS.2019.8898510>, 2019a.
- 98 Touzi, R., Pawley, S., Hosseini, M., and Jiao, X.: Polarimetric L-band PALSAR2 for Discontinuous Permafrost  
99 Mapping In Peatland Regions, in: *IGARSS 2019 - 2019 IEEE International Geoscience and Remote Sensing*  
00 *Symposium, IGARSS 2019 - 2019 IEEE International Geoscience and Remote Sensing Symposium*,  
01 *Yokohama, Japan, xvii–ccxxii*, <https://doi.org/10.1109/IGARSS.2019.8900243>, 2019b.
- 02 Tsuyuzaki, S., Iwahana, G., and Saito, K.: Tundra fire alters vegetation patterns more than the resultant  
03 thermokarst, *Polar Biol.*, 41, 753–761, <https://doi.org/10.1007/s00300-017-2236-7>, 2018.
- 04 Ullmann, T., Banks, S. N., Schmitt, A., and Jagdhuber, T.: Scattering Characteristics of X-, C- and L-Band  
05 PolSAR Data Examined for the Tundra Environment of the Tuktoyaktuk Peninsula, Canada, *Appl. Sci.*, 7,  
06 595, <https://doi.org/10.3390/app7060595>, 2017.
- 07 Vincent, W. F., Callaghan, T. V., Dahl-Jensen, D., Johansson, M., Kovacs, K. M., Michel, C., Prowse, T., Reist,  
08 J. D., and Sharp, M.: Ecological Implications of Changes in the Arctic Cryosphere, *AMBIO*, 40, 87–99,  
09 <https://doi.org/10.1007/s13280-011-0218-5>, 2011.
- 10 Walker, B., Wilcox, E. J., and Marsh, P.: Accuracy assessment of late winter snow depth mapping for tundra  
11 environments using Structure-from-Motion photogrammetry1, *Arct. Sci.*, [https://doi.org/10.1139/as-2020-](https://doi.org/10.1139/as-2020-0006)  
12 0006, 2020.
- 13 Walker, X. J., Rogers, B. M., Baltzer, J. L., Cummings, S. R., Day, N. J., Goetz, S. J., Johnstone, J. F., Turetsky,  
14 M. R., and Mack, M. C.: ABoVE: Wildfire Carbon Emissions and Burned Plot Characteristics, NWT, CA,  
15 2014-2016, ORNL DAAC, <https://doi.org/10.3334/ORNLDAAC/1561>, 2018a.
- 16 Walker, X. J., Rogers, B. M., Baltzer, J. L., Cumming, S. G., Day, N. J., Goetz, S. J., Johnstone, J. F., Schuur, E.  
17 A. G., Turetsky, M. R., and Mack, M. C.: Cross-scale controls on carbon emissions from boreal forest  
18 megafires, *Glob. Change Biol.*, 24, 4251–4265, <https://doi.org/10.1111/gcb.14287>, 2018b.
- 19 Walker, X. J., Baltzer, J. L., Laurier, W., Cumming, S. G., Day, N. J., Goetz, S. J., Johnstone, J. F., Potter, S.,  
20 Rogers, B. M., Schuur, E. a. G., Turetsky, M. R., and Mack, M. C.: ABoVE: Characterization of Carbon  
21 Dynamics in Burned Forest Plots, NWT, Canada, 2014, ORNL DAAC,  
22 <https://doi.org/10.3334/ORNLDAAC/1664>, 2019a.
- 23 Walker, X. J., Baltzer, J. L., Cumming, S. G., Day, N. J., Ebert, C., Goetz, S., Johnstone, J. F., Potter, S., Rogers,  
24 B. M., Schuur, E. A. G., Turetsky, M. R., and Mack, M. C.: Increasing wildfires threaten historic carbon sink  
25 of boreal forest soils, *Nature*, 572, 520–523, <https://doi.org/10.1038/s41586-019-1474-y>, 2019b.
- 26 Whalen, D., Forbes, D. L., Hopkinson, C., Lavergne, J. C., Manson, G. K., Marsh, P., and Solomon, S. M.:  
27 Topographic LiDAR-Providing a new perspective in the Mackenzie Delta, 2009.



- 28 Whitley, M., Frost, G. V., Jorgenson, M. T., Macander, M., Maio, C. V., and Winder, S. G.: ABoVE: Permafrost  
29 Measurements and Distribution Across the Y-K Delta, Alaska, 2016, ORNL DAAC,  
30 <https://doi.org/10.3334/ORNLDAAC/1598>, 2018a.
- 31 Whitley, M. A., Frost, G. V., Jorgenson, M. T., Macander, M. J., Maio, C. V., and Winder, S. G.: Assessment of  
32 LiDAR and Spectral Techniques for High-Resolution Mapping of Sporadic Permafrost on the Yukon-  
33 Kuskokwim Delta, Alaska, *Remote Sens.*, 10, 258, <https://doi.org/10.3390/rs10020258>, 2018b.
- 34 Wilcox, E. J., Keim, D., Jong, T. de, Walker, B., Sonnentag, O., Sniderhan, A. E., Mann, P., and Marsh, P.:  
35 Tundra shrub expansion may amplify permafrost thaw by advancing snowmelt timing, *Arct. Sci.*,  
36 <https://doi.org/10.1139/as-2018-0028>, 2019.
- 37 Wilson, C., Dann, J., Bolton, R., Charsley-Groffman, L., Jafarov, E., Musa, D., and Wullschleger, S.: In Situ Soil  
38 Moisture and Thaw Depth Measurements Coincident with Airborne SAR Data Collections, Barrow and  
39 Seward Peninsulas, Alaska, 2017, <https://doi.org/10.5440/1423892>, 2021.
- 40 Woodward, A. and Beever, E. A.: Conceptual ecological models to support detection of ecological change on  
41 Alaska National Wildlife Refuges, 2011.
- 42 Yi, Y., Kimball, J. S., Chen, R. H., Moghaddam, M., Reichle, R. H., Mishra, U., Zona, D., and Oechel, W. C.:  
43 Characterizing permafrost active layer dynamics and sensitivity to landscape spatial heterogeneity in Alaska,  
44 *The Cryosphere*, 12, 145–161, <https://doi.org/10.5194/tc-12-145-2018>, 2018.
- 45 Zhang, Y., Touzi, R., Feng, W., Hong, G., Lantz, T. C., and Kokelj, S. V.: Landscape-scale variations in near-  
46 surface soil temperature and active-layer thickness: Implications for high-resolution permafrost mapping,  
47 *Permafr. Periglac. Process. J.*, 2021. <https://doi.org/10.1002/ppp.2104>
- 48 Zhao, Y., Chen, R.H., Bakina-Dogaheh, K., Whitcomb, J., Yi, Y., Kimball, J. S., Moghaddam, M.: Mapping  
49 Boreal Forest Species and Canopy Height using Airborne SAR and Lidar Data in Interior Alaska, IGARSS  
50 2022 - 2022 IEEE International Geoscience and Remote Sensing Symposium, Kuala Lumpur, Malaysia,  
51 2022, pp. 4955-4958, doi: 10.1109/IGARSS46834.2022.9883311.
- 52  
53  
54